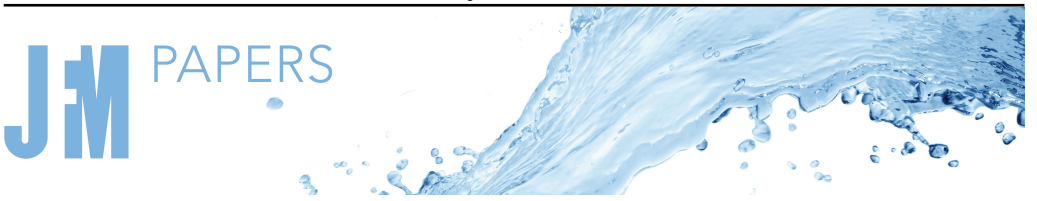
J. Fluid Mech. (2025), *vol.* 1022, A44, doi:10.1017/jfm.2025.10744



Focusing patterns of spherical particles in a viscoelastic flow through square channels

Hiroshi Yamashita[1], **Yuta Miki**[2], **Daisuke Yoneyama**[2], **Kento Higashi**[2], **Takuma Tsukasa**[2], **Yoshiyuki Tagawa**[3], **Naoto Yokoyama**[4], **Tomoaki Itano**[2] **and Masako Sugihara-Seki**[2]

[1]Graduate School of Integrated Sciences for Life, Hiroshima University, Higashihiroshima, Hiroshima 739-8521, Japan

[2]Department of Pure and Applied Physics, Kansai University, Suita, Osaka 564-8680, Japan

[3]Department of Mechanical Systems Engineering, Tokyo University of Agriculture and Technology, Koganei, Tokyo 184-8588, Japan

[4]Department of Mechanical Engineering, Tokyo Denki University, Adachi, Tokyo 120-8551, Japan

Corresponding author: Hiroshi Yamashita, hyamashi@hiroshima-u.ac.jp

(Received 31 January 2025; revised 22 August 2025; accepted 12 September 2025)

The inertial migration of neutrally buoyant spherical particles in viscoelastic fluids flowing through square channels is experimentally and numerically studied. In the experiments, using dilute aqueous solutions of polymers with various concentrations that have nearly constant viscosities, we measured the distribution of suspended particles in downstream cross-sections for the Reynolds number (Re) up to 100 and the elasticity number (El) up to 0.07. There are several focusing patterns of the particles, such as four-point focusing near the centre of the channel faces on the midlines for low El and/or high Re, four-point focusing on the diagonals for medium El, single-point focusing at the channel centre for relatively high El and low Re, and five-point focusing near the four corners and the channel centre for high El and very low Re. Among these focusing patterns, various types of particle distributions suggesting the presence of a new equilibrium position located between the midline and the diagonal, and multistable states of different equilibrium positions were observed. In general, as El increases from 0 at a constant Re, the particle focusing positions shift from the midline to the diagonal in the azimuthal direction first, and then inward in the radial direction to the channel centre. These focusing patterns and their transitions were numerically well reproduced based on a FENE-P model with measured values of viscosity and relaxation time. Using the numerical results, the experimentally observed focusing patterns of particles are elucidated in terms of the fluid elasticity-induced lift and the wall-induced elastic lift.

Key words: particle/fluid flows, viscoelasticity, microfluidics

© The Author(s), 2025. Published by Cambridge University Press.

https://doi.org/10.1017/jfm.2025.10744 Published online by Cambridge University Press

1. Introduction

Particle migration in laminar channel flows has been intensively studied because of its importance in many academic and industrial fields. In particular, cross-stream migration due to inertia or viscoelasticity of suspending fluids has gathered considerable attention as a basis for passive separation and sorting of biological cells and microparticles in microfluidic devices (Di Carlo *et al.* 2007; Leshansky *et al.* 2007). Under the effects of inertia or viscoelasticity, suspended particles migrate laterally towards specific positions in the channel cross-section, depending on the flow condition and channel geometry (Matel & Toner 2014; Zhou & Papautsky 2020). If the focusing positions and/or cross-stream migration velocities can be controlled by the size, shape and deformability of the suspended particles, this phenomena can be used for particle separation and sorting in label-free and external field-free ways using microchannels of simple geometry. To this end, extensive studies have been conducted to develop novel microfluidic devices suitable for target cells as well as to understand the underlying mechanisms of particle migration (e.g. Di Carlo 2009; Zhang *et al.* 2016; Stoecklein & Di Carlo 2019; Razavi Bazaz *et al.* 2020; Tang *et al.* 2020; Kalyan *et al.* 2021; Lee, Kim & Yang 2023; Zhang *et al.* 2024). However, the fundamentals of particle migration under the effects of inertia and fluid viscoelasticity, and their interplay have not been fully understood. In the present study, focusing on the combined effects of inertia and fluid viscoelasticity, we experimentally and numerically investigate the inertial migration of rigid spherical particles in viscoelastic fluids flowing through a straight channel with square cross-sections. To avoid complications arising from interparticle interactions such as excluded-volume effects (Kazerooni *et al.* 2017), hydrodynamic repulsive motion between neighbouring particles (Udono 2020) and their train formation (Matas *et al.* 2004*a*; Humphry *et al.* 2010; Hur, Tse & Di Carlo 2010; Kahkeshani, Haddadi & Di Carlo 2016; Del Guidice *et al.* 2018; D'Avino & Maffettone 2020; Hu *et al.* 2022), we consider dilute suspensions in which such interactions can be neglected.

Inertial migration was first reported by Segré & Silberberg (1961) for neutrally buoyant spherical particles suspended in circular tube flows of a Newtonian fluid. They observed that suspended particles migrate laterally towards an annulus whose radius is 0.6 times as large as the tube radius at relatively low Reynolds numbers (Re) (Segré & Silberberg 1961, 1962). This phenomenon, referred to as the Segré–Silberberg (SS) effect, is caused by the presence of lifts due to inertia, and the particle focusing annulus is called the SS annulus (Matas, Morris & Guazzelli 2004*b*). Subsequent theoretical studies elucidated that the inertial lifts consist mainly of a shear gradient-induced lift acting in the higher shear direction (i.e. towards the tube wall) and a wall effect acting in the direction away from the tube wall (Ho & Leal 1974; Schonberg & Hinch 1989; Asmolov 1999). The balance between these two competing lifts determines the radius of the SS annulus (Matas, Morris & Guazzelli 2009). In channels with rectangular cross-sections, which are commonly used in microfluidics, suspended particles migrate towards a discrete set of equilibrium positions in the channel cross-section (Di Carlo *et al.* 2007; Bhagat, Kuntaegowdanahalli & Papautsky 2008; Kim & Yoo 2008; Di Carlo *et al.* 2009). This property is beneficial for the design of cell separation devices. Several experimental and numerical studies reported two-phase properties of the inertial migration of spherical particles in square channel flows; in the first phase, they rather rapidly migrate mostly in the radial direction towards a ring, and then in the second stage, they move slowly along the ring towards four points located near the centre of the channel faces (Choi, Seo & Lee 2011; Abbas *et al.* 2014; Nakagawa *et al.* 2015). This ring of the focusing particles corresponds to the SS annulus, so that it is termed the pseudo Segré–Silberberg (pSS) ring, and the final focusing position

https://doi.org/10.1017/jfm.2025.10744 Published online by Cambridge University Press

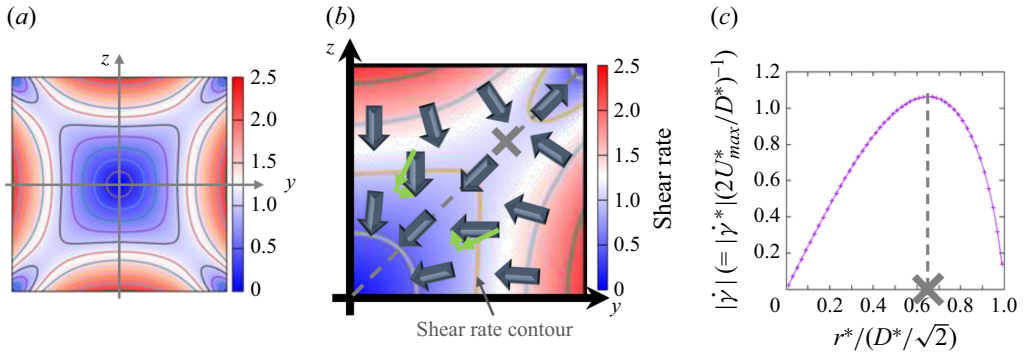


Figure 1. (*a*) The contours of the shear rate $|\dot{\gamma}|$ in the square cross-section of a pressure-driven flow of a Newtonian fluid without suspended particles, (*b*) approximate directions of $-\nabla|\dot{\gamma}|$ in the first quadrant of the cross-section, and (*c*) the profile of the shear rate along the diagonal (dashed line in panel *b*). The shear rate is normalised by $2U^*_{max}/D^*$, where U^*_{max} is the maximum flow velocity. The cross-mark represents the location of the maximum shear rate on the diagonal.

is termed the channel face equilibrium position or the midline equilibrium position (MEP) (Miura, Itano & Sugihara-Seki 2014; Shichi *et al.* 2017; Yu *et al.* 2019). The final focusing on the MEP in square channel flows can be explained by a balance between two major lifts due to inertia; the shear gradient-induced lift in the direction towards higher shear and the wall effect away from the channel wall (Matas, Morris & Guazzelli 2004*c*). The contours of the shear rate $|\dot{\gamma}|$ for the pressure-driven flow through a square channel and approximate directions of the shear gradient $-\nabla|\dot{\gamma}|$ in the first quadrant of the cross-section are plotted in figures 1(*a*) and (*b*), respectively. Because the shear gradient-induced lift exerts from lower shear to higher shear, their directions are nearly opposite to the arrows in figure 1(*b*), which are mostly outward in the radial direction and away from the diagonal (i.e. towards the y, z axes (midlines)) in the azimuthal direction. This lift is dominant in the region apart from the channel wall, while the wall effect is superposed near the channel wall. The radial component of the lift is larger than the azimuthal component for most of the cross-section, and thus, suspended particles first move in an approximately radial direction towards the pSS ring, where the resultant lift normal to the ring vanishes. The particles then move slowly along the pSS ring due to the azimuthal component of the shear gradient-induced lift towards the midline until reaching the midline at the MEP.

Particle focusing on the MEP can be observed for rather small particle-to-channel width ratios (blockage ratios) and relatively low Re. The blockage ratio is defined as $\kappa = d^*/D^*$, where d^* and D^* represent the diameter of the spherical particles and the width of the channel, respectively. In this paper, the dimensional quantities are denoted by a superscript $*$. The Reynolds number is defined as $Re = \rho^* U^* D^*/\mu^*$, where ρ^* and μ^* respectively represent the density and viscosity of the fluid and U^* is the average flow velocity. The particle Reynolds number is defined as $Re_p = Re \times \kappa^2$. In the cases of $\kappa \gtrapprox 0.2$ and/or $Re \gtrapprox 200$, other types of particle focusing patterns emerge in square channel flows of Newtonian fluids, depending on κ and Re (Prohm & Stark 2014; Miura *et al.* 2014).

Particle migration in viscoelastic fluids has also long been studied. Mason and his coworkers observed complex behaviours of particles suspended in viscoelastic fluids, depending on the fluid rheology; rigid spherical particles migrate inward in highly elastic fluids flowing through a circular tube, whereas the migration direction is inverted in a predominantly shear-thinning fluid (Karnis & Mason 1966; Gauthier, Goldsmith & Mason

https://doi.org/10.1017/jfm.2025.10744 Published online by Cambridge University Press

1971). Recent microfluidic studies also reported various intricate phenomena of particle migration in viscoelastic fluids related to shear-thinning effects and secondary flows, and these effects tend to weaken the effect of fluid elasticity (for details, see review articles on viscoelastic microfluidics such as D'Avino & Maffettone (2015), D'Avino *et al.* (2017), Lu *et al.* (2017), Yuan *et al.* (2018), Zhou & Papautsky (2020) and the references therein). Thus, to simplify the problem, the present study mainly considers the effect of fluid elasticity on the inertial migration of particles when the fluid viscosity is nearly constant and secondary flow is almost negligible. In the experiments, the present study uses dilute aqueous solutions of polyvinylpyrrolidone (PVP), a biocompatible polymer, whose viscosity is almost independent of the shear rate. For viscoelastic fluids, the Weissenberg number $Wi = \lambda^* U^*/D^*$, qualifying the ratio of elastic force to viscous force, is added as an important parameter controlling the particle migration behaviour, where λ^* represents the relaxation time of the fluid. The ratio between Wi and Re gives the elasticity number $El = Wi/Re = \lambda^* \mu^*/(\rho^* D^{*2})$, which depends only on the channel dimension and fluid properties.

Most previous studies on the particle cross-stream migration under the effect of fluid elasticity have mainly investigated the cases of negligible inertia and non-negligible but small inertia. In general, the lift due to the fluid elasticity originates from the normal stress differences. Specifically, the first normal stress difference N_1, which is defined as the difference between the streamwise normal stress and the transverse normal stress in the shear direction, is dominant when the secondary flow can be neglected. In curvilinear shear flow, N_1, representing a tension in the streamwise direction, gives a rise to a volume force termed the hoop stress acting on the fluid in the direction of the curvature (Steinberg 2021). In the case of negligible inertia and small blockage ratios, Ho & Leal (1976) theoretically indicated that the fluid elasticity-induced lift drives a spherical particle towards the lower shear region when suspended in two-dimensional (2-D) unidirectional shear flow of a second-order fluid. Based on their result of the tension proportional to the square of the shear rate, they explained that bowed streamlines on both sides of a particle suspended in a flow with a shear gradient such as a Poiseuille flow generate a lift in the direction of decreasing shear. This explanation is in line with a previous study by Karnis & Mason (1966), who reported that spherical particles in viscoelastic fluids flowing through circular tubes migrate towards the tube centreline at very low Re. This inward migration of suspended particles was accounted for by larger lift towards the tube centreline than that towards the tube wall because of increasing normal stress with increasing radial distance from the centreline.

The fluid elasticity-induced lift exerting in the direction of lower shear is also consistent with the experimental results in microfluidics. Leshansky *et al.* (2007) observed that spherical particles suspended in 8 wt % PVP solutions flowing through a nearly 2-D channel (a rectangular channel with a large aspect ratio ≈ 22) migrate towards the middle plane of the channel. In addition, they demonstrated that the width of the particle distribution can be controlled by varying the particle size and altering the elasticity and/or viscosity of the suspending medium. In square channel flows, spherical particles in 8 wt % PVP solutions were reported to focus near four corners as well as the centre of the cross-section at very low Re (Yang *et al.* 2012; Seo, Kang & Lee 2014). The middle plane of the 2-D channel and the centre and four corners in the square cross-section correspond to the lowest shear regions; as seen from figure 1(*c*), there is a position of maximum shear midway between the centre and the corner along the diagonal, and the minimum shear attains at the centre and four corners. Approximate directions of decreasing shear are represented by arrows in figure 1(*b*). Here, we refer to the particle focusing position at the centre as the axial equilibrium position (AEP) and near the corners as the corner

https://doi.org/10.1017/jfm.2025.10744 Published online by Cambridge University Press

equilibrium position (CEP). In the case of negligible inertia for square channel flows, focusing on the closest CEP or AEP depending on the particle's initial position was also reported for numerical simulations when the second normal stress difference was negligible (Villone *et al.* 2013).

When the inertia is not negligible in square channel flows, an increase in wall effect, acting in the direction away from the channel wall, diminishes the particle focusing near the corners (CEP) (Yang *et al.* 2011; Seo *et al.* 2014; Kim & Kim 2016). As a result, suspended particles achieve a single-position focusing near the channel centreline (AEP). This transition from five-position focusing to one-position focusing by increasing the flow rate was also shown by numerical studies (Raoufi *et al.* 2019). The single-position focusing holds great potential for application such as flow cytometry (Del Guidice *et al.* 2013).

To realise a high throughput in microfluidic devices, however, the effect of inertia increases with increasing Re. Since the inertial lift due to the shear gradient is directed nearly opposite to the lift due to the fluid elasticity as noted above, the particle migration behaviour in viscoelastic fluids at finite Re should be largely affected by the interplay between inertia and elasticity. There are few previous studies on the particle migration in viscoelastic fluids at larger Re, with the exception of a few studies. Lim *et al.* (2014) performed an experimental study employing hyaluronic acid solutions in which suspended particles in a square channel flow migrate towards the channel centreline over a wide range of Reynolds numbers $10 \leqslant Re \leqslant 10^4$ at $El \sim 0.1$. Li, McKinley & Ardekani (2015) numerically simulated the migration of a spherical particle located on the midline of the square cross-section of the channel at lower El. Their results based on the Oldroyd-B model showed that particle focusing on the channel centre occurs in flows with strong elasticity and weak inertia, and that there exists a critical elasticity number El ($\sim O(0.01)$) above which the particle migrates to the centre. The Oldroyd-B model, which has a parameter β, the ratio of the solvent viscosity to the total viscosity, in addition to Re and Wi (or El), is often used for polymer solutions. Li *et al.* (2015) adopted $\beta = 0.1$. Yu *et al.* (2019) performed numerical computations of trajectories of a spherical particle in square channel flows of an Oldroyd-B model at $\beta = 0.5$ in the ranges of $\widehat{Re}$ up to 100 and $\widehat{Wi}$ up to 1.5. Here, the hat indicates that the parameter is defined in terms of maximum flow velocity rather than average flow velocity. Note that $Re \approx \widehat{Re}/2.1$ and $Wi \approx \widehat{Wi}/2.1$ for Newtonian fluids. Showing the existence of an equilibrium position on the diagonal (named here diagonal equilibrium position, DEP) and its coexistence with the MEP or the CEP, they illustrated a map of the particle focusing pattern as a function of Re and El at $\kappa = 0.15$. It was demonstrated that, as the fluid elasticity increases at finite and constant Re, particle focusing emerges successively from the MEP to the DEP and then to the CEP and the AEP (Yu *et al.* 2019). Hu *et al.* (2024) reported a similar conclusion for a numerical study of ellipsoidal particles suspended in a square channel flow of Oldroyd-B fluids at $\kappa = 0.2$.

In our previous study (Yokoyama *et al.* 2021), we experimentally and numerically investigated the inertial focusing of spherical particles in viscoelastic fluids flowing through square channels at $Re = 50$ and $\kappa = 0.15$. Micro-scale experiments using dilute PVP aqueous solutions reported for the first time the observation of the particle focusing on four points of the DEP and that, as the PVP concentration increases, the focusing position transitions from the MEP to the DEP, with a bistable state of the MEP and DEP in between. The PVP concentrations were so low that we could not measure the relaxation time of the PVP solutions using a rotational rheometer. Thus, although the Weissenberg number was unknown for each case, numerical computations based on the finitely extensible nonlinear elastic-Peterlin (FENE-P) model qualitatively reproduced these

https://doi.org/10.1017/jfm.2025.10744 Published online by Cambridge University Press

focusing patterns under the assumption that Wi increases with increasing PVP concentration. Additionally, subtracting the lift on a particle at finite Wi from that at $Wi = 0$ located at the same position, we evaluated approximately the lift due to the fluid elasticity, and found that the distribution of the estimated lift in the channel cross-section is similar to that due to N_1 except near the channel wall. The direction of the lift is inward in the radial direction and towards the diagonal in the azimuthal direction in the region apart from the channel wall. Note that $N_1 \propto |\dot{\gamma}|^{\alpha}$ $(1 < \alpha \leqslant 2)$ (Leshansky *et al.* 2007) and $-\boldsymbol{\nabla}|\dot{\gamma}|^{\alpha}$ is parallel to $-\boldsymbol{\nabla}|\dot{\gamma}|$, it is reasonable that this direction agrees with the arrows in figure 1(*b*), which represent the decreasing shear directions. Thus, it was shown that the fluid elasticity-induced lift exerting in the direction towards lower shear, which was derived theoretically in 2-D unidirectional shear flow of a second-order fluid for small blockage ratios with negligible inertia (Ho & Leal 1976), is approximately valid in the case of finite blockage ratios and finite Re in square channel flows at least at relatively small Wi. Furthermore, the analysis of the conformation tensor demonstrated that outward lift exerts on a particle close to the channel wall, due to the polymer elongation in the region between the particle and the channel wall. This lift was termed the wall-induced elastic lift and the transition of the particle focusing pattern observed experimentally and numerically was accounted for by the competition between the lift due to N_1 and the wall-induced elastic lift.

In the inertial migration, the interplay between inertia and fluid elasticity is unclear yet. In this paper, both experiments and numerical simulations where characteristic parameters are systematically varied are performed, and the variation of lift due to the rheological characteristics of the working fluids is investigated. This study presents a variety of focusing patterns of particles, caused by the interplay between the inertial lift and fluid elasticity-induced lift. In the experiments, our previous study (Yokoyama *et al.* 2021) is extended to wider ranges of PVP concentration ϕ (= 0–4.0 wt %) and Re (= 1–100). The PVP concentration was still lower than that in other previous studies (Leshansky *et al.* 2007; Yang *et al.* 2011; Del Guidice *et al.* 2013; Seo *et al.* 2014), but the relaxation time could be successfully measured using an extensional rheometry, which enabled the evaluation of Wi and El. The obtained focusing patterns of the particles are illustrated as a function of Re and El. Along with the MEP, DEP, CEP and AEP, we have newly found the presence of an intermediate equilibrium position (IEP); particles are focused on eight points located at intermediate positions between the MEP and DEP, symmetric with respect to the midline. Furthermore, the experiments have demonstrated the presence of new bistable states such as the DEP and the AEP or IEP, in addition to the DEP and MEP already reported in Yu *et al.* (2019) and Yokoyama *et al.* (2021), and the CEP and AEP reported previously (Yang *et al.* 2011; Kim *et al.* 2012; Seo *et al.* 2014; Kim & Kim 2016). In particular, as the PVP concentration increases from 0 at a constant Re (= 20), the particle focusing position shifts successively from the MEP to the IEP, then the DEP, the DEP and AEP, and the AEP alone. Numerical simulations using the FENE-P model are performed with rheologically measured values of the PVP solutions (Re, El and β). The numerical simulations successfully reproduced these focusing patterns observed in the experiments with similar rheological parameters. The numerically obtained lift map for each case is used to account for the particle focusing pattern and its transition. The effect of the fluid elasticity on the inertial focusing is discussed in terms of the fluid elasticity-induced lift due to N_1 and the wall-induced elastic lift.

This paper is organised as follows. Section 2 describes the experimental method used to observe particles suspended in a square channel flow of PVP aqueous solutions, and outlines the numerical method for calculating the net lift acting on a particle in a viscoelastic flow based on the FENE-P model. In § 3 we present various particle

https://doi.org/10.1017/jfm.2025.10744 Published online by Cambridge University Press

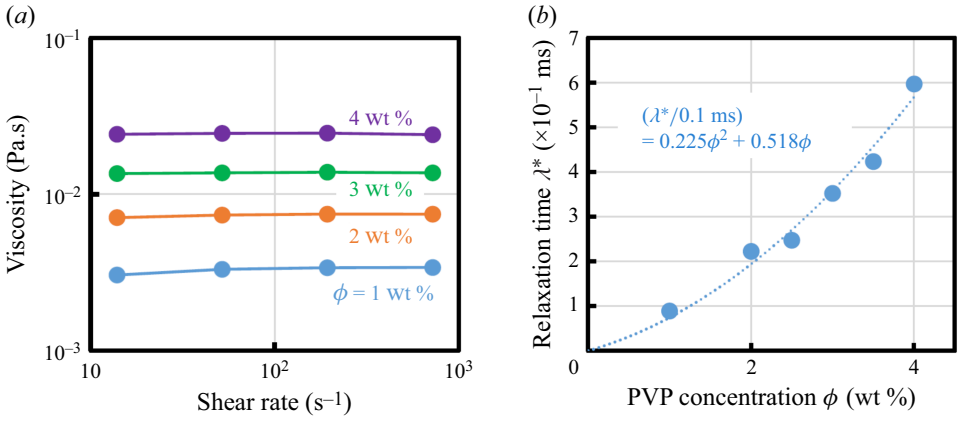


Figure 2. (*a*) Viscosity and (*b*) relaxation time of PVP solutions measured using a rotational rheometer (Haake Mars III) and dripping-onto-substrate capillary break-up extensional rheometry (CaBER-DoS), respectively (all experiments performed at 22 °C).

distributions in the channel cross-section, provide numerical results corresponding to the experimental observations, and compare these results with findings from other studies. Finally, § 4 concludes the paper by summarising the main results.

2. Material and methods

2.1. *Experimental methods*

Spherical polystyrene particles (Thermo Scientific) with a mean diameter $d^* = 60$ μm (59.6 ± 0.8 μm) were suspended at volume fractions of 0.003–0.01 % in aqueous solutions of PVP. The volume fraction of the particles is so low that hydrodynamic interactions between particles can be neglected. The solutions contain PVP ($Mw = 360$ kDa, Tokyo Chemical Industry) at the concentrations of $\phi = 0$–4.0 wt %, and the density was adjusted to the particle density $\rho^* = 1.05 \times 10^3$ kg m^{-3} by adding sodium chloride. The viscosity μ^* and relaxation time λ^* of the solutions were measured, using a rotational rheometer (HAAKE MARS III) and a dripping-onto-substrate capillary breakup extensional rheometry (CaBER-DoS) (Dinic, Jimenez & Sharma 2017; Sur & Rothstein 2018; Franco-Gómez *et al.* 2021; Rubio *et al.* 2022), respectively (figure 2). As shown in figure 2, the viscosities are nearly constant, independent of the shear rate, i.e. the shear thinning is not clearly seen. This is because the dilute PVP aqueous solutions were used. The relaxation times are so small that the viscoelastic property is weak. The rheological data are summarised in table 1.

Figure 3(*a*) shows the experimental set-up. A syringe pump (Nexus 6000, ISIS) was used to infuse the suspension through a straight glass tube (VitroCom) with a square cross-section of width $D^* = 400$ μm and various lengths L^* (= 20–600 mm). The glass tube was immersed in a tank filled with the suspending fluid, in order to match the refractive index of the inside and outside of the tube. The cross-section of the channel 1–2 mm upstream of the outlet was illuminated with an LED light (U-technology UFLS-751) and imaged from the downstream side along the centre axis of the channel using a high-speed camera (Photron FASTCAM mini AX100, Nova S12) equipped with a long-working-distance objective (Olympus SLMPLN 20×) at a frame rate of 50–13 600 frames/s. As the volume fraction of the particles is low, they appear individually on the images (figure 3*b*). The images obtained were analysed with the public domain software ImageJ (NIH, USA) to yield the position of each particle centre in the cross-section. The pixel size was typically

https://doi.org/10.1017/jfm.2025.10744 Published online by Cambridge University Press

PVP ϕ (wt %)	μ^* (mPa s)	λ^* (ms)	β	El	Wi at $Re = 20$
0	1.12	0	1	0	0
0.5	1.59	3.15×10^{-2}	7.0×10^{-1}	3.0×10^{-4}	6.0×10^{-3}
1.0	2.78	7.43×10^{-2}	4.0×10^{-1}	1.2×10^{-3}	2.5×10^{-2}
1.5	4.54	1.28×10^{-1}	2.4×10^{-1}	3.5×10^{-3}	6.9×10^{-2}
2.0	6.87	1.94×10^{-1}	1.6×10^{-1}	7.9×10^{-3}	1.6×10^{-1}
2.5	9.76	2.70×10^{-1}	1.1×10^{-1}	1.6×10^{-2}	3.2×10^{-1}
3.0	13.2	3.58×10^{-1}	8.3×10^{-2}	2.8×10^{-2}	5.6×10^{-1}
3.5	17.2	4.57×10^{-1}	6.4×10^{-2}	4.7×10^{-2}	9.4×10^{-1}
4.0	21.8	5.67×10^{-1}	5.0×10^{-2}	7.4×10^{-2}	1.47

Table 1. Viscosity μ^*, relaxation time λ^*, viscosity ratio β, elasticity number El and Weissenberg number Wi (at $Re = 20$) of PVP aqueous solutions at 22 °C.

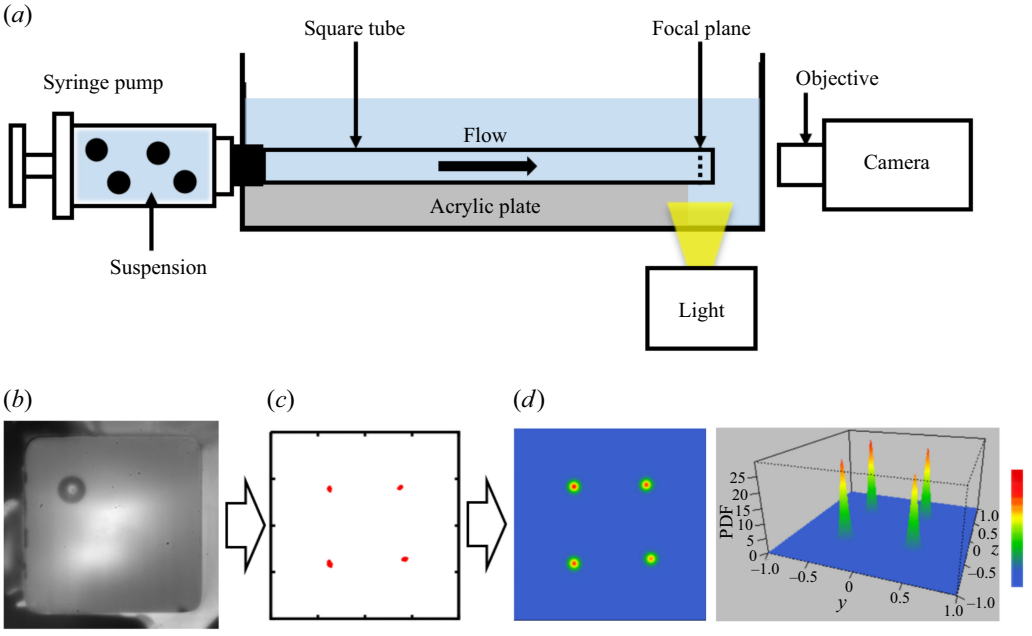


Figure 3. (*a*) Experimental set-up, (*b*) a typical image, (*c*) superimposition of particle positions, and (*d*) PDFs of particles in the channel cross-section.

≈ 0.995 μm pixel^{-1}. In each experiment, the positions of more than 300 particles were detected to obtain the distribution of the particles in the cross-section by superimposition and their probability densities (figures 3*c* and 3*d*).

In the present study, the blockage ratio was $\kappa = d^*/D^* = 0.15$. The Reynolds number ranged from 1 to 100, corresponding to a particle Reynolds number ($= Re \times \kappa^2$) from 0.02 to 2.25. The PVP concentration $\phi = 0$–4.0 wt % corresponds to an elasticity number ranging from 0 to 0.07 (table 1).

2.2. *Numerical methods*

Numerical computations were performed based on the FENE-P model to find the lift distribution and the focusing positions, which are sinks of the vector field of the lift.

https://doi.org/10.1017/jfm.2025.10744 Published online by Cambridge University Press

The governing equations non-dimensionalised by the mean flow velocity and the channel width are written as

$$\nabla \cdot \boldsymbol{u} = 0, \tag{2.1}$$

$$\frac{\partial \boldsymbol{u}}{\partial t} + (\boldsymbol{u} \cdot \nabla)\boldsymbol{u} = -\nabla p + \frac{\beta}{Re}\nabla^2 \boldsymbol{u} + \nabla \cdot \boldsymbol{T}_p + \boldsymbol{f}_{IB} - G\boldsymbol{e}_x, \tag{2.2}$$

where $\boldsymbol{u}$, p and $\boldsymbol{T}_p$ are respectively the flow velocity, the pressure and the viscoelastic stress tensor derived from the polymers. Here, the x axis is taken along the centreline of the channel, and the y and z axes normal to the side walls. In (2.2), $1/Re$ is the dimensionless total shear viscosity and the ratio of the solvent viscosity to the zero shear rate viscosity of the solution is expressed by β. The interaction between the inertial particles and the fluid flow is modelled by the volume force $\boldsymbol{f}_{IB}$ according to the immersed boundary method (Kajishima *et al.* 2001). The flow is driven by the mean pressure gradient $-G\boldsymbol{e}_x$, so that the volume flux is constant. The magnitude of the mean pressure gradient G is dynamically determined by the parameter adaptive control, and it is almost constant in the final steady states.

The viscoelastic stress tensor $\boldsymbol{T}_p$ is modelled by the FENE-P model to mimic the viscoelastic properties of the PVP aqueous solution (Purnode & Crochet 1998), though the shear thinning is not clear in the dilute PVP aqueous solutions as shown in figure 2(*a*). In fact, the numerical results shown below will be independent of the selection of the FENE-P model because the sensitivity of the flow fields to the selection of constitutive models is known to be small for small $Wi \leqslant 0.32$ (see, for example, Herrchen & Öttinger 1997; Peng *et al.* 2023; John *et al.* 2024). Among the constitutive models, the FENE-P model is widely used in numerical simulations of viscoelastic shear flows due to its relative simplicity and accuracy in predicting macroscopic properties of dilute polymer solutions (Yamani & McKinley 2023).

In this paper, $\boldsymbol{T}_p$ is given by the positive-definite symmetric conformation tensor $\boldsymbol{C}$ as

$$\boldsymbol{T}_p = -\frac{1-\beta}{ReWi}\left[\boldsymbol{I} - \frac{\boldsymbol{C}}{1 - tr(\boldsymbol{C})/l^2}\right], \tag{2.3}$$

and the time evolution of $\boldsymbol{C}$ is given as

$$\frac{\partial \boldsymbol{C}}{\partial t} = -(\boldsymbol{u} \cdot \nabla)\boldsymbol{C} + \boldsymbol{C} \cdot \nabla \boldsymbol{u} + (\nabla \boldsymbol{u})^T \cdot \boldsymbol{C} + \frac{1}{Wi}\left[\boldsymbol{I} - \frac{\boldsymbol{C}}{1 - tr(\boldsymbol{C})/l^2}\right]. \tag{2.4}$$

Here, the maximal length of the polymers normalised by their equilibrium length l is set to be 100. As noted below, the numerical results presented in this paper are hardly affected by the value of l, as long as l is larger than about 15. The square-root symmetric tensor $\boldsymbol{B}$ instead of $\boldsymbol{C} = \boldsymbol{B}^2$ is employed for numerical stability (Balci *et al.* 2011), and then the governing equation of $\boldsymbol{B}$ is written as

$$\frac{\partial \boldsymbol{B}}{\partial t} = -(\boldsymbol{u} \cdot \nabla)\boldsymbol{B} + \boldsymbol{B} \cdot \nabla \boldsymbol{u} + \boldsymbol{A} \cdot \boldsymbol{B} + \frac{1}{2Wi}\left[\boldsymbol{B}^{-1} - \frac{\boldsymbol{B}}{1 - tr(\boldsymbol{B}^2)/l^2}\right], \tag{2.5}$$

where $\boldsymbol{A}$ is the antisymmetric tensor that satisfies $\boldsymbol{A} \cdot \boldsymbol{B} + \boldsymbol{B} \cdot \boldsymbol{A} = (\nabla \boldsymbol{u})^T \cdot \boldsymbol{B} - \boldsymbol{B} \cdot \nabla \boldsymbol{u}$.

These governing equations (2.1)–(2.3) and (2.5) are numerically integrated by a fractional-step method (see Kajishima *et al.* (2001) for details of the numerical method) with time increment $\Delta t = 10^{-4}$. The spatial derivatives are evaluated by the fourth-order central difference with $\Delta x = \Delta y = \Delta z = 1/128$. The Poisson equation for the pressure is solved by the biconjugate gradient stabilised (BiCGSTAB) method. The periodic boundary

https://doi.org/10.1017/jfm.2025.10744 Published online by Cambridge University Press

condition was used in the streamwise direction (the x direction) with a period length $L_x = 2$.

To evaluate the lift acting on the rigid particle, we consider the case that the particle is fixed in the lateral direction (the y and z directions) while they travel in the streamwise direction (the x direction) and rotate freely. Thus, we have equations for the streamwise velocity U_C of the centre of mass of the particle $\boldsymbol{x}_C$ and the angular velocity $\boldsymbol{\Omega}_C$ as

$$\frac{\pi}{6}\kappa^3\frac{\mathrm{d}U_C}{\mathrm{d}t} = \int(-f_{IBx})\mathrm{d}V, \quad \frac{\pi}{60}\kappa^5\frac{\mathrm{d}\boldsymbol{\Omega}_C}{\mathrm{d}t} = \int(\boldsymbol{x}-\boldsymbol{x}_C)\times(-\boldsymbol{f}_{IB})\mathrm{d}V. \tag{2.6}$$

The lift acting on the particles is given by

$$\boldsymbol{F} = (F_y, F_z), \quad F_i = \int(-f_{IBi})\mathrm{d}V, \quad i = y, z. \tag{2.7}$$

The lift $\boldsymbol{F}$ is non-dimensionalised by $\rho^* U^{*2} D^{*2}$ in this formulation.

Corresponding to our experiments at $Re = 20$, we performed computations for $\kappa = 0.15$, $El = 0$–0.016 and $Wi = 0$–0.32 (see table 1). Here, we note that the dimensionless lateral flow velocity is smaller than 10^{-6} in the absence of the particle in the parameter ranges examined, and the secondary flow is negligible. Thus, the lift due to the flow–particle interactions solely determines the lateral motion of the particle and equilibrium positions in the cross-section of the channel.

The appropriateness of the grid spacing and the periodic boundary length was verified. We compared the lift force acting on the particle at $(y, z) = (0.17, 0.17)$ in the simulation when $Re = 20$ and $El = 0.016$ for grid spacings of 1/128 and 1/192. The former is 3.675×10^{-4} while the latter is 3.574×10^{-4}, and the difference is smaller than 3 % (see figure S1 in the supplementary material is available at https://doi.org/10.1017/jfm.2025.10744). The periodic length $L_x = 2$ was determined based on the error assessment of the numerical computation as noted in Yokoyama *et al.* (2021).

With regard to the maximum polymer length l, it is not straightforward to estimate the value of l. One estimate is provided by a microscopic formula (Clasen *et al.* 2006), which gives l for the PVP solution as larger than about 25 when the physical properties of the polymers are adopted from the literature (Abdel Azim *et al.* 1992; Kamli, Guettari & Tajouri 2023). Because the PVP solutions used in the present experiments were dilute, we consider that l could be even larger. Therefore, we chose to set $l = 100$. The value of l has little effect on the flow field as far as $tr(\boldsymbol{C}) \ll l^2$. From the results of the computation we found that the maximal values of $tr(\boldsymbol{C})$ for $El = 0.0003$ and 0.016 at $Re = 20$ are approximately 3 and 20, respectively. This implies that the condition of maximum $tr(\boldsymbol{C}) \ll l^2$ is satisfied in the whole parameter range. This indicates that the rheological characteristics of the fluid do not depend on the detailed value of l as far as l is set to be much larger than about 15 in the current computation. In fact, the difference in lift force acting on the particle at $(y, z) = (0.17, 0.17)$ for a simulation in which having $Re = 20$ and $El = 0.016$ is 4 % between $l = 25$ and $l = 100$, but is 20 % between $l = 10$ and $l = 100$. Thus, the present choice of $l = 100$ well represents the PVP rheological property in the FENE-P model.

3. Results and discussion

3.1. *Experimental results*

As representative examples of the experimental results for small inertia and finite elasticity of suspending fluids, figure 4 shows the development of the particle distribution along the

https://doi.org/10.1017/jfm.2025.10744 Published online by Cambridge University Press

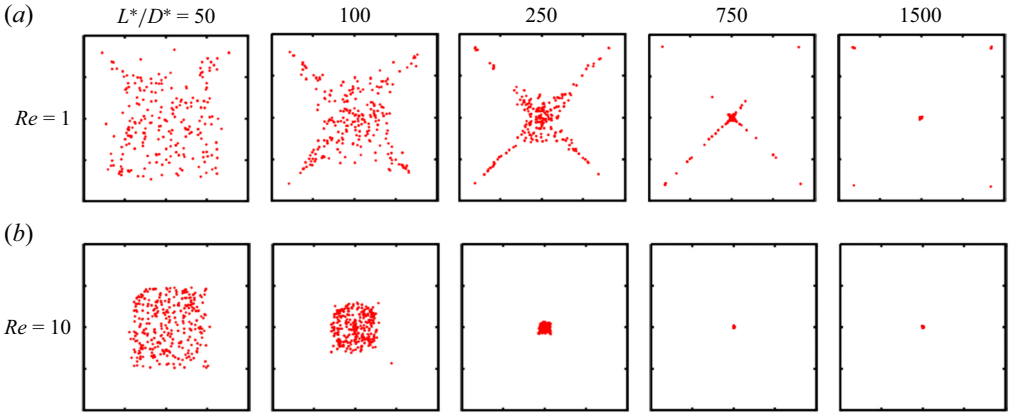


Figure 4. Distributions of particles at (*a*) $Re = 1$ and (*b*) $Re = 10$ for various L^*/D^* at $\phi = 4.0$ wt % and $\kappa = 0.15$. The particles positions are superimposed in each figure.

streamwise direction from the channel inlet for $\phi = 4.0$ wt % at $Re = 1$ and 10. Each dot represents the position of the particle centre in the channel cross-section. Note that figure 4 displays the superimposed particle positions instead of the snapshot. The cumulative particle distribution for lager L^*/D^* corresponds to that in a cross-section located farther downstream from the inlet. At $Re = 1$ shown in figure 4(*a*), suspended particles are widely dispersed in the most upstream cross-section, moving inward towards the centre except near the diagonals and finally focusing at four points near the corners (CEP) as well as the centre (AEP) in the most downstream cross-section. This focusing pattern is consistent with that reported by Seo *et al.* (2014) for spherical particles suspended in PVP solutions at $\phi = 8.0$ wt % and $Re = 0.55$ and 1.11 ($\kappa = 0.1, 0.17$). As noted in the introduction, particle focusing on these locations can be accounted for if the fluid elasticity-induced lift is directed to the lower shear region (figure 1*b*). At $Re = 10$ shown in figure 4(*b*), suspended particles move inward and eventually solely focus on the channel centre (AEP). The focusing on the CEP shown in figure 4(*a*) disappears owing to enhanced wall effects directed away from the channel wall. This single-position focusing due to the synergetic effect of inertia and fluid elasticity is termed elasto-inertial focusing (Yang *et al.* 2011).

Figure 5(*a–g*) illustrates the inertial migration of particles at a finite Re ($= 20$) for various PVP concentrations of $\phi = 0$–3.0 wt % ($El = 0$–0.028, $Wi = 0$–0.56). Figure 5(*h*) shows probability density functions (PDFs) of more than 300 particles in the most downstream cross-section ($L^*/D^* = 1500$) for each ϕ. Figure 5(*a*) represents the case in a Newtonian fluid. Suspended particles are dispersed with relatively higher concentrations near a ring (pSS ring) in the most upstream cross-section, and further downstream they are first aligned along the pSS ring and then gradually migrate to four points near the centre of the channel faces (MEP). These developments of the particle distribution agree with previous experimental results observed in Newtonian fluids at relatively low Re, though the particle focusing in the present study at $Re = 20$ is slower than that reported at higher Re (Shichi *et al.* 2017).

For $\phi = 0.5$ wt % shown in figure 5(*b*), suspended particles are fairly widely dispersed in the most upstream cross-section, but remain mostly distributed along the pSS ring even in the most downstream cross-section. Probability densities in the most downstream cross-section ($L^*/D^* = 1500$) in figure 5(*h*) indicate that particles show higher concentrations near eight points on the pSS ring (circles in figure 5*b*), located slightly off the midlines and symmetric with respect to the midlines. In addition, the probability densities on the

https://doi.org/10.1017/jfm.2025.10744 Published online by Cambridge University Press

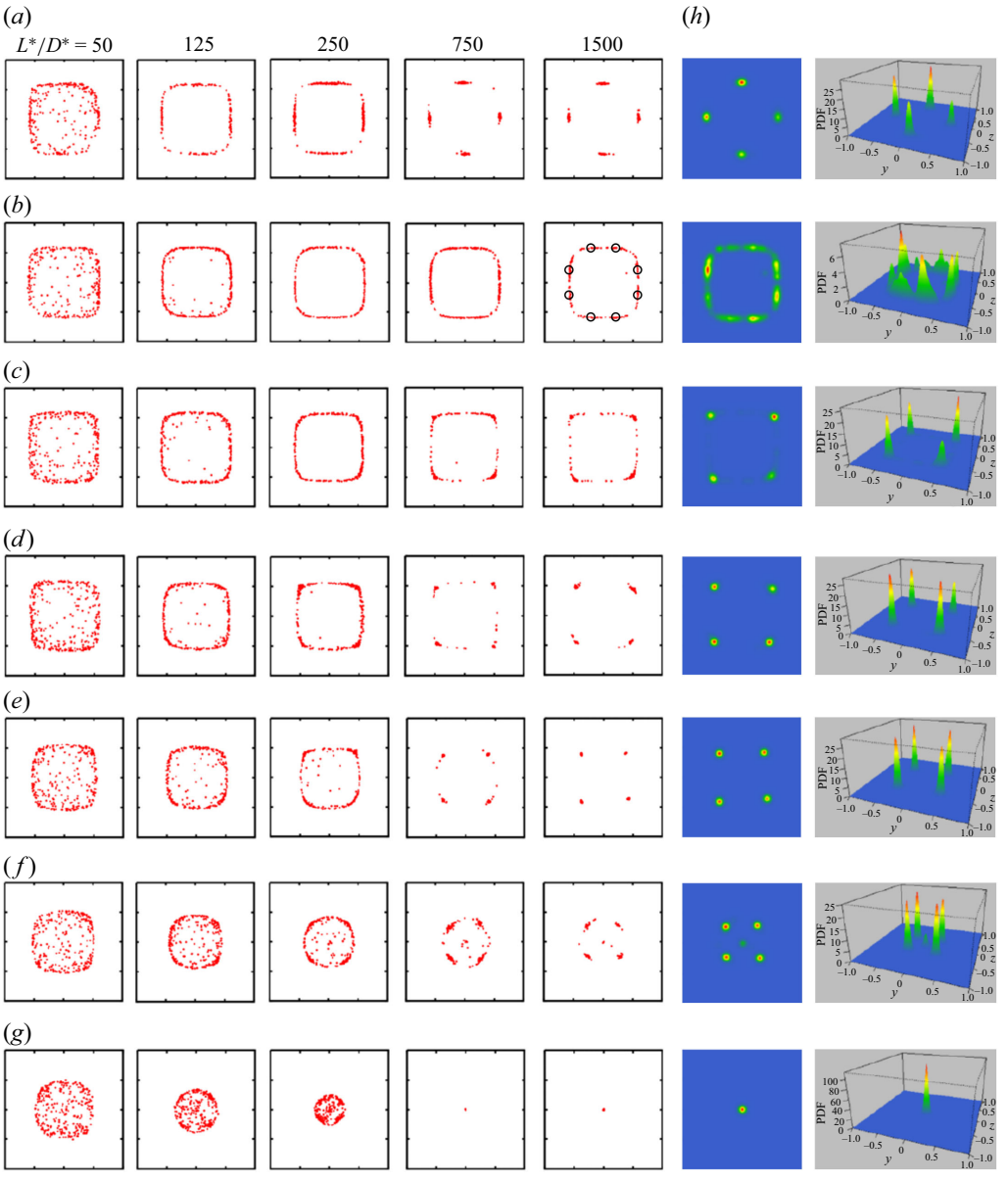


Figure 5. (*a–g*) Distributions of particles for $L^*/D^* = 50$–1500 at (*a*) $\phi = 0$, (*b*) 0.5 wt %, (*c*) 1.0 wt %, (*d*) 1.5 wt %, (*e*) 2.0 wt %, (*f*) 2.5 wt % and (*g*) 3.0 wt %. (*h*) Probability density functions for $L^*/D^* = 1500$. Here $\kappa = 0.15$ and $Re = 20$.

midlines and the diagonals in the most downstream cross-section are smaller than those in the second most downstream cross-section ($L^*/D^* = 750$). If the channel is long enough, particles are expected to focus on these points. Thus, this position is named the IEP. The present numerical simulation has reproduced this focusing pattern with parameter values comparable to this experimental condition, as shown below.

At $\phi = 1.0$–2.0 wt % shown in figure 5(*c–e*), particles approach the pSS ring as they move downstream, and eventually focus near four points located on the diagonals (DEP), with the final positions closer to the centre for larger ϕ. At $\phi = 2.5$ wt % shown in

https://doi.org/10.1017/jfm.2025.10744 Published online by Cambridge University Press

figure 5(*f*), the centre in the cross-section (AEP) is added as the final focusing position. At $\phi = 3.0$ wt % in figure 5(*g*), particles migrate monotonically towards the AEP.

The probability densities of particles shown in figure 5(*h*) indicate that an increase in PVP concentration transitions the final focusing positions of particles from the MEP to the IEP, the DEP and then to the AEP. There are several important features observed in the particle distributions and the probability densities. Firstly, the inertial migration in PVP solutions also exhibit two-phase properties, similar to that in Newtonian fluids. In the first phase they rapidly migrate towards the pSS ring and in the second phase they slowly move along the pSS ring towards stable equilibrium positions. The stable equilibrium positions on the pSS ring are the MEP in figures 5(*a*), the IEP in figure 5(*b*) and the DEP in figure 5(*c–e*). Secondly, as ϕ increases, the final focusing positions shift from the midline to the diagonal in the azimuthal direction, such as from the MEP, to the IEP and then the DEP (figure 5*a–c*), and then move in the radial direction towards the channel centre (AEP), as shown in figure 5(*c–g*). This transition is understood from an increase in the fluid elasticity-induced lift due to the first normal stress difference N_1, which exerts in the direction towards the diagonal and inward in the square cross-section, as discussed above (figure 1*b*). For particles located near the channel wall, the fluid elasticity also generates outward lift (wall-induced elastic lift), due to polymer elongation upstream between the particle and the channel wall. The competition between the lift due to N_1 directed mostly inward and the wall-induced elastic lift directed mostly outward is associated with the tendency for the equilibrium positions to change only in the azimuthal direction not in the radial direction for small ϕ (figure 5*a–c*), as discussed below. This feature is also reproduced by the present numerical simulation. Thirdly, the presence of the IEP is observed for the first time in the viscoelastic flow in the present study. Our previous study (Yokoyama *et al.* 2021) reported the presence of a MEP and DEP coexistence state at higher Re ($= 50$) between the MEP focusing and DEP focusing. As shown below in figures 6 and 7, this is also true in the present study. At lower Re ($= 20$), however, instead of this bistable state, a new state where only the IEP is stable emerges. In these transition states, the lift on the pSS ring is so small that the particle migration in the second phase is extremely slow, which is shown below for the present numerical simulation. As a result, long distances from the channel inlet are necessary for particles to focus on stable equilibrium positions. This is the reason why particles are observed to be aligned along almost the entire pSS ring even in the most downstream cross-section (figure 5*b*). Lastly, another coexistence state of the DEP and AEP is observed at $\phi = 2.5$ wt %. This state appears between the DEP focusing (figure 5*e*) and the AEP focusing (figure 5*g*).

Figure 6 shows the particle distributions observed at various Re and ϕ in the most downstream cross-section ($L^*/D^* = 1500$). Let us see the variation of the particle focusing pattern with Re for each ϕ. For $\phi = 0$, the suspending fluid is a Newtonian fluid. In Newtonian fluids, no lift acts on spherical particles when the inertia is negligible . Thus, at low Re, the migration of particles is so slow that they are rather widely dispersed with higher concentrations along the pSS ring even at $L^*/D^* = 1500$. Increasing Re intensifies focusing on four points of the MEP due to an increase in inertial lift, which agrees with previous studies (Shichi *et al.* 2017).

For $\phi = 0.5$ wt %, a slight effect of fluid elasticity can be seen at low Re, where particles are nearly aligned along the pSS ring. Although it is difficult to specify the locations of higher concentrations at $Re = 1$ (figure 6*a*), probability densities show a higher concentration near intermediate positions located between the diagonal and midline (IEP) in the range of $5 \leqslant Re \leqslant 25$, as already seen in figure 5(*b*) at $Re = 20$. As Re increases, the locations of higher concentration move from the diagonal to the midline (see figure 6(*b*) at $Re = 10$ and figure 5(*b*) at $Re = 20$), until at $Re = 30$ particles are

https://doi.org/10.1017/jfm.2025.10744 Published online by Cambridge University Press

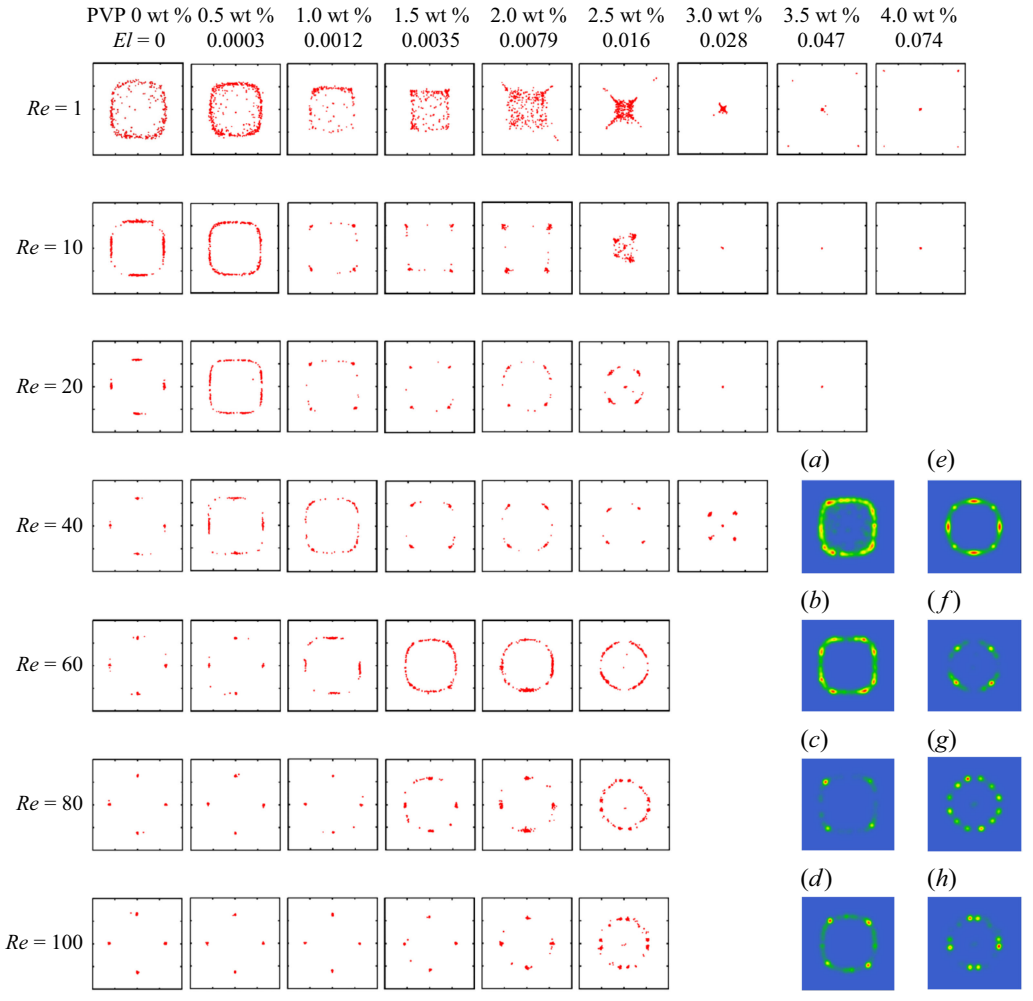


Figure 6. Distributions of particles for various ϕ and Re ($\kappa = 0.15$, $L^*/D^* = 1500$). Probability density functions for (*a*) $\phi = 0.5$ wt %, $Re = 1$, (*b*) $\phi = 0.5$ wt %, $Re = 10$, (*c*) $\phi = 1$ wt %, $Re = 40$, (*d*) $\phi = 1.5$ wt %, $Re = 60$, (*e*) $\phi = 2$ wt %, $Re = 60$, (*f*) $\phi = 2.5$ wt %, $Re = 60$, (*g*) $\phi = 2.5$ wt %, $Re = 70$ and (*h*) $\phi = 2.5$ wt %, $Re = 100$.

focused near the midlines (MEP). At larger $Re(\geqslant 40)$, the particle focusing positions are readily seen to be the MEP.

For low ϕ ($0 < \phi \leqslant 2$ wt %), particles are focused on four points of the DEP at Re lower than a certain critical Re, Re_1, and the MEP at Re higher than another critical Re, Re_2. In the range of Re between Re_1 and Re_2, the final particle focusing positions are eight points of the IEP for $\phi = 0.5$ wt %. For $\phi = 1.0$–2.0 wt %, both of Re_1 and Re_2 increase with increasing ϕ, and at Re between these two values, particles show higher concentrations both near the diagonal and near the midline (see figures 6*d* and 6*e*), suggesting a bistable state of the DEP and MEP.

The variation of the particle distribution observed for $\phi = 2.5$ wt % is quite unique. Focusing on four points of the DEP is observed in the Re range from 30 to 60 (see figure 6(*f*) at $Re = 60$), below which particles are focused on the AEP as well, representing a bistable state of the DEP and AEP. At very low Re ($\leqslant 5$), particles are solely focused on

https://doi.org/10.1017/jfm.2025.10744 Published online by Cambridge University Press

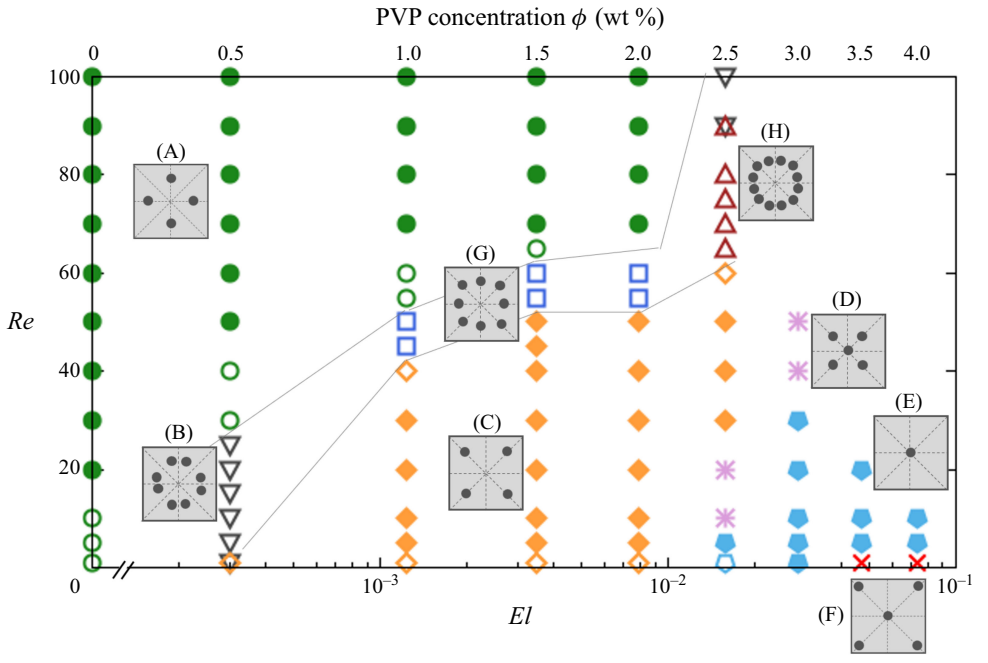


Figure 7. Particle focusing patterns; type (A): circles, type (B): inverted triangles, type (C): diamonds, type (D): asterisks, type (E): pentagons, type (F): crosses, type (G): squares and type (H): triangles. Filled marks represent the case where particles are focused or nearly focused on equilibrium positions, and open marks represent the case where the focusing pattern is inferred from PDFs. Here $\kappa = 0.15$ and $L^*/D^* = 1500$.

the AEP. On the other hand, above this range ($Re > 60$), particles are focused on four points of the DEP and eight points of the IEP, for a total of twelve points, representing another bistable state of the DEP and IEP (see figure 6*g*). In this bistable state, an increase in Re weakens focusing on the DEP and strengthens focusing on the IEP, until only a few particles are seen near the diagonals at $Re \geqslant 90$ (see figure 6(*h*) at $Re = 100$).

For $\phi \geqslant 3.0$ wt %, experiments at larger Re could not be carried out owing to limitations of the experimental equipment caused by increased solution viscosity and, hence, pressure. At $Re = 1$, particles are solely focused on the AEP for $\phi = 3.0$ wt %, but on four points near the corners (CEP) as well for $\phi = 3.5$ and 4.0 wt %. At $Re \geqslant 5$, particles show a single focusing on the AEP except for the cases of $\phi = 3.0$ wt % at $Re \geqslant 40$. In the excluded cases, particles are focused on four points of the DEP as well.

The particle focusing patterns observed experimentally at $L^*/D^* = 1500$ are summarised as a function of Re and El (lower abscissa) or PVP concentration ϕ (upper abscissa) in figure 7. As schematically shown in figure 7, eight different focusing patterns are obtained (labelled A–H), depending on the number and positions of the particle focusing: (A) four points of the MEP, (B) eight points of the IEP, (C) four points of the DEP, (D) four points of the DEP and the AEP (a total of five points), (E) single point of the AEP, (F) four points of the CEP and the AEP (a total of five points), (G) four points of the DEP and four points of the MEP (a total of eight points) and (H) four points of the DEP and eight points of the IEP (a total of twelve points). Except for types (D) and (F), filled marks in figure 7 represent the case where particles are focused or nearly focused on equilibrium positions, and open marks represent the case where focusing is not sufficient and the focusing pattern is inferred from probability densities. Two open marks

https://doi.org/10.1017/jfm.2025.10744 Published online by Cambridge University Press

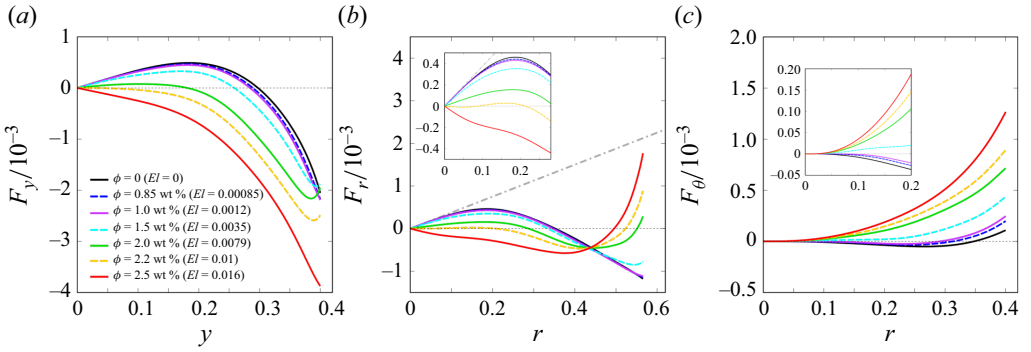


Figure 8. Numerical results for the radial component of the lift exerted on the particle located (*a*) on the midline and (*b*) on the diagonal. The azimuthal component of the lift on the particle located (*c*) on the line $z = y\tan(\pi/8)$. Here $\kappa = 0.15$ and $Re = 20$.

are superposed in two cases of $\phi = 0.5$ wt %, $Re = 1$ and $\phi = 2.5$ wt %, $Re = 90$, where it is difficult to identify the focusing pattern, as noted above.

In figure 7, inertia is dominant and fluid elasticity is small in the upper left, whereas in the lower right, fluid elasticity is dominant and inertia is small. From the top left to the bottom right, the particle focusing pattern is seen to shift approximately in the order of the type (A), (C), (E), and (F). Between types (A) and (C), type (B) emerges at low Re and ϕ, whereas type (G) appears at higher Re and ϕ, and type (H) at even higher Re and ϕ. Between types (C) and (E), type (D) appears. In types (B), (G) and (H), very small lifts on the pSS ring (see figure 9(*c*) for type (B)) cause very slow motion of particles in the second phase, resulting in their alignment almost all around the pSS ring even in the most downstream cross-section of the experiments. Therefore, the focusing patterns are unclear and inferred from PDFs.

3.2. *Numerical results*

Table 1 summarises the parameter values obtained from the measurements of the viscosity and relaxation time of the PVP solutions used in the experiments. Using these values, we conducted numerical computations of the lift acting on a spherical particle in square channel flows of a FENE-P model, corresponding to the experiments for various PVP concentrations ϕ at $Re = 20$ and $\kappa = 0.15$, shown in figure 5.

Figures 8(*a*) and 8(*b*) plot the radial component of lift F_r acting on the particle placed on the midline (the y axis) and the diagonal. Note that $F_r = F_y$ on the y axis. The lift in Newtonian flows is directed outward, i.e. $F_r > 0$ near the channel centre, while $F_r < 0$ near the channel wall (Di Carlo *et al.* 2009; Nakagawa *et al.* 2015). As ϕ (or El) increases, F_r decreases except on the diagonal near the channel wall, i.e. corners, which is due to increasing fluid elasticity-induced lift (see the introduction). In the range $0 < \phi \leqslant 1$ wt % ($0 < El \leqslant 0.0012$), the F_r curves nearly overlap and the zeros of F_r move only slightly. Note that these zeros correspond to the MEP (figure 8*a*) and the DEP (figure 8*b*) because $F_\theta = 0$ on these lines. As ϕ (or El) increases further, F_r continues to decrease except near the corners where F_r increases significantly. For $\phi = 2.2$ wt % ($El = 0.01$), F_r remains close to 0 at $0 \leqslant r \lessapprox 0.2$ both on the midline and the diagonal. Beyond this value ($\phi > 2.2$ wt %, $El > 0.01$), F_r becomes negative except near the corners, leading to the disappearance of the MEP and DEP. Instead, the channel centre (AEP) becomes a stable equilibrium position, and another focusing position (CEP) appears near the corner outside of the saddle position where the particle almost touches the two walls.

https://doi.org/10.1017/jfm.2025.10744 Published online by Cambridge University Press

Similarly, figure 8(*c*) plots the azimuthal component of lift F_θ acting on the particle placed on a line of $z = y\tan(\pi/8)$. The lift in Newtonian flows is directed away from the diagonal, i.e. towards the midline ($F_\theta < 0$ in figure 8*c*), in a region apart from the channel wall, as noted in the introduction. Near the channel wall, it is directed in the opposite direction ($F_\theta > 0$ in figure 8*c*) and F_θ has a zero midway between the channel centre and the wall. As ϕ (or El) increases, F_θ increases monotonically, which is due to increasing fluid elasticity-induced lift (see the introduction), and the zeros of F_θ approach the origin. Between $\phi = 1.0$ wt % ($El = 0.0012$) and 1.5 wt % ($El = 0.0035$), these zeros vanish; above this value, $F_\theta > 0$ on the entire line of $z = y\tan(\pi/8)$ and the lift acts towards the diagonal. This is the case where the fluid elasticity-induced lift exceeds the inertial lift in the azimuthal direction.

Most of the above mentioned properties of F_r and F_θ in figure 8 at $Re = 20$ are commonly seen at $Re = 50$ (Yokoyama *et al.* 2021). Additionally, it may be interesting to note that four more features of the lift are seen in figure 8. Firstly, near the channel centre ($r \lessapprox 0.1$), F_r on the midline and F_r on the diagonal are very close to each other and F_θ is nearly equal to zero. This is explained from the fact that the flow field is almost axisymmetric in the region far apart from the channel wall. Secondly, for $\phi \leqslant 1$ wt %, an increase in ϕ decreases zeros of F_r only slightly (figures 8*a* and 8*b*), whereas it decreases zeros of F_θ significantly (figure 8(*c*)). This feature is related to the tendency experimentally observed for the equilibrium positions to move only in the azimuthal direction not in the radial direction for small ϕ (figure 5*a–c*). Thirdly, for $\phi = 2.2$ wt %, F_r is negative on the entire midline (figure 8*a*), whereas F_r on the diagonal changes its sign three times between the centre and the corner, i.e. F_r has three zeros on the diagonal (inset of figure 8*b*). Fourthly, this implies that at approximately this ϕ (= 2.2 wt %), the fluid elasticity-induced lift exceeds the inertial lift in the radial direction. It is interesting that this occurs at higher ϕ in the radial direction than in the azimuthal direction. Thus, it is suggested that the fluid elasticity-induced lift has a larger azimuthal component than the radial component, compared with the inertial lift.

The distributions of lift in the cross-section and trajectories of particles as well as equilibrium positions are shown in figure 9. The top half of each plot is a lift map, where each arrow represents the direction of the lift acting on a particle located at the arrow's origin and the magnitude is shown by the colour. The solid line represents the contour of $F_r = 0$, and the dashed line the contours of $F_\theta = 0$. For low ϕ, the contour of $F_r = 0$ (r nullcline) forms a closed loop around the centre, whereas the contours of $F_\theta = 0$ consist of the midlines (the y and z axes), the diagonals and a closed loop. Although all the contours of $F_\theta = 0$ are nullclines, here we refer only to the closed loop as θ nullcline for convenience because F_θ is always 0 on the midlines and the diagonals.

The bottom half of figure 9 shows the trajectories of the particle centre starting from various positions (cross-marks), projected on the cross-section. The magnitude of the lift along the trajectories is indicated by the colour. The trajectories of the particles and their colour in figure 9(*a–e*) highlight distinct features of the two-phase properties of the inertial migration. In the first phase they mainly migrate in the radial direction towards the pSS ring under the lift $\sim O(10^{-4})$ and in the second phase they migrate along the pSS ring under the small lift $\sim O(10^{-5})$ or less, except for the case in figure 9(*e*). If these lifts are balanced with the Stokes drag, the migration velocities are estimated to be $\sim O(10^{-3})$ and $O(10^{-4})$ or less, respectively. In addition, figure 9(*a–e*) shows that the pSS ring is located very close to the r nullcline. When the r and θ nullclines are close to each other, as in figure 9(*c*), the lift on the pSS ring is extremely small ($\sim O(10^{-6})$), resulting in very small migration velocities ($\sim O(10^{-5})$). This explains the experimentally obtained distribution of particles in figure 5(*b*) and the experimental difficulty in identifying the

https://doi.org/10.1017/jfm.2025.10744 Published online by Cambridge University Press

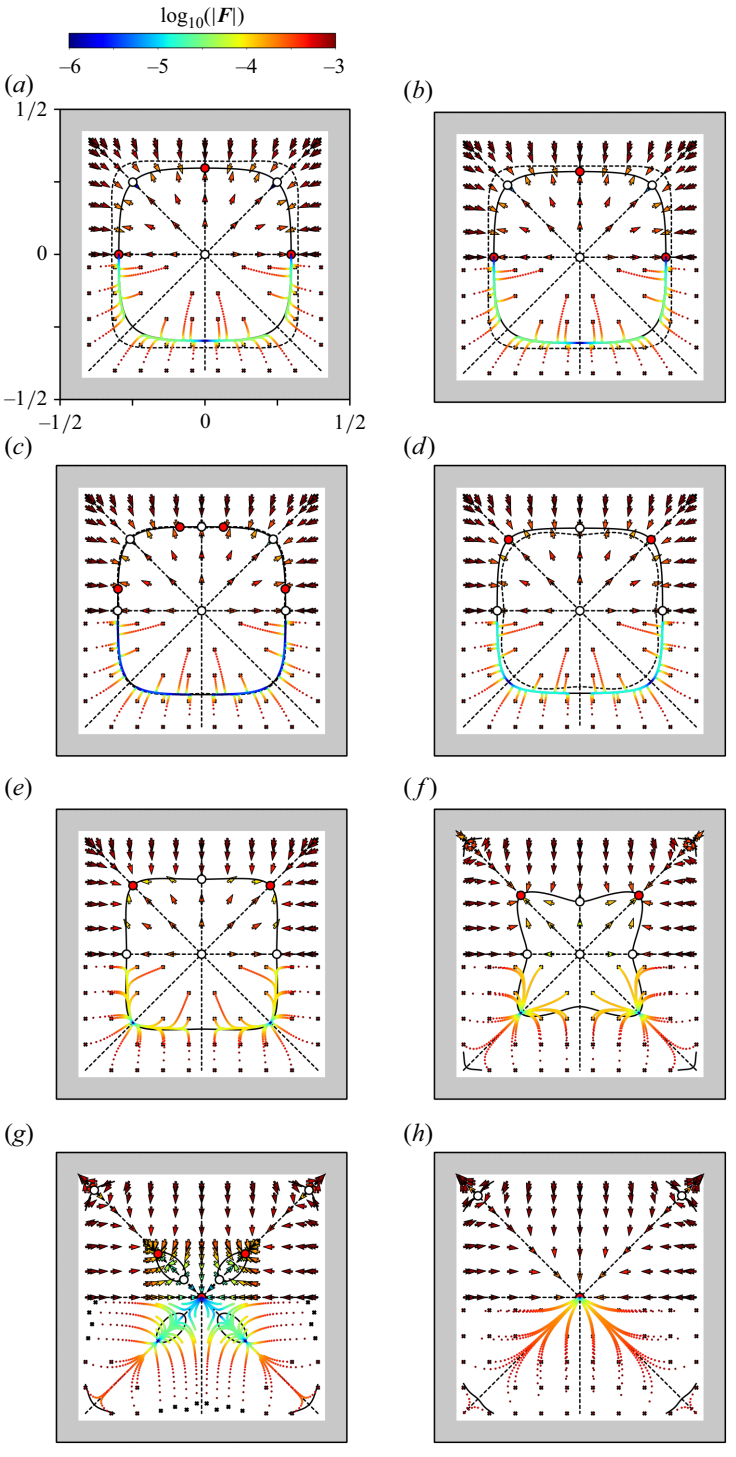


Figure 9. Numerical results of lifts, equilibrium positions, nullclines (r nullcline: solid lines, θ nullcline: dashed lines) and particle trajectories for (*a*) $\phi = 0$ ($El = 0$, $\beta = 1$), (*b*) 0.5 wt % ($El = 0.0003$, $\beta = 0.7$), (*c*) 0.85 wt % ($El = 0.00085$, $\beta = 0.47$), (*d*) 1.0 wt % ($El = 0.0012$, $\beta = 0.4$), (*e*) 1.5 wt % ($El = 0.0035$, $\beta = 0.24$), (*f*) 2.0 wt % ($El = 0.0079$, $\beta = 0.16$), (*g*) 2.2 wt % ($El = 0.01$, $\beta = 0.14$) and (*h*) 2.5 wt % ($El = 0.016$, $\beta = 0.11$). Here $\kappa = 0.15$ and $Re = 20$.

https://doi.org/10.1017/jfm.2025.10744 Published online by Cambridge University Press

type (B) focusing pattern in figure 7. On the other hand, when the θ nullcline is absent as in figure 9(*e*), the lift on the pSS ring is $\sim O(10^{-4})$ or less, which remains slightly smaller than that in the first phase. In the cases with larger ϕ (figure 9*f*–*h*), the trajectories exhibit characteristics different from those described earlier. There is no distinct second phase, which is shown in figure 9(*a*–*e*), and the trajectories do not form the pSS ring.

In figure 9, stable, saddle and unstable equilibrium positions are also displayed, and the focusing positions observed experimentally correspond to the stable equilibrium positions. The intersections between the zero contours of F_r and F_θ represent the equilibrium positions where lift vanishes; the intersection between the r nullcline and the midlines corresponds to the MEP, and that between the r nullcline and the diagonal corresponds to the DEP. From the symmetry, the channel centre is always an equilibrium position (AEP). The lift directions around the channel centre together with the particle trajectories indicate that the AEP is an unstable equilibrium position in figure 9(*a*–*f*) ($El = 0$–0.0079), while it is a stable equilibrium position in figures 9(*g*) and 9(*h*) ($El = 0.01, 0.016$). From these results along with F_r curves in figures 8(*a*) and 8(*b*), the critical El is estimated to be ≈ 0.01. The present experiments shown in figure 7 confirm this critical El (~ 0.01) from boundaries between type (C) and (E) or (D). In addition, this value is equal to that obtained by previous numerical studies (Li *et al.* 2015; Yu *et al.* 2019). In their studies, numerically obtained critical El is explained from a balance between the inertial lift and the elasticity-induced lift. We discuss this issue below.

Figure 9(*a*) shows the case of a Newtonian fluid, where the θ nullcline is located outside of the r nullcline (Yamashita, Itano & Sugihara-Seki 2019). Here F_r is positive inside the r nullcline, whereas F_r is negative outside of it. Similarly, F_θ is negative inside the θ nullcline, whereas F_θ is positive outside of it in $0 < \theta < \pi/4$, and *vice versa* in $\pi/4 < \theta < \pi/2$. The direction of the lift in the region away from the channel wall, outward and towards the midline, coincides with that of the shear gradient-induced lift, in the direction of increasing shear as mentioned in the introduction. In figure 9(*a*) ($\phi = 0$), since the MEP and DEP are located inside the θ nullcline where F_θ is directed towards the midline, the MEP is a stable equilibrium position while the DEP is a saddle point. This predicts that particles focus on the MEP, corresponding to the type (A) focusing pattern. This focusing pattern agrees with the present experiment for $\phi = 0$ (figure 5*a*) and previous studies for spherical particles in Newtonian fluids (Di Carlo *et al.* 2007, 2009; Choi *et al.* 2011; Miura *et al.* 2014; Nakagawa *et al.* 2015; Shichi *et al.* 2017).

Figure 9(*a*–*e*) shows that, as ϕ increases, an increase in fluid elasticity moves the θ nullcline inward, whereas the r nullcline located inside the θ nullcline at $\phi = 0$ does not largely change its position. These features are consistent with the lift profiles in figure 8, where the zeros of the F_r curves, r nullclines, hardly move and the zeros of F_θ curves, θ nullclines, shift inwards for $\phi \leqslant 1$ wt %. Since the θ nullcline approaches closer to the r nullcline along the midline than along the diagonal (see figure 9*b*), these two nullclines cross near the midline (see figure 9*c*). Thus, a pair of intersections representing another equilibrium position emerges near the midline as shown in figure 9(*c*). This new equilibrium position corresponds to the IEP. In figure 9(*c*) ($\phi = 0.85$ wt %) the lift map indicates that the IEP is stable, but the MEP is changed to be a saddle point, representing the type (B) focusing pattern. This focusing pattern agrees with the experiment for $\phi = 0.5$ wt %, showing particle focusing on eight points of the IEP (figure 5*b*), though the present numerical simulation for $\phi = 0.5$ wt % (figure 9*b*) predicts that the MEP remains stable. In the numerical simulation, ϕ needs to be slightly larger for the IEP to appear. A further increase in ϕ ($\geqslant 1.0$ wt %) moves the θ nullcline even closer to the channel centre so that the θ nullcline is completely inside the r nullcline as in figure 9(*d*) ($\phi = 1.0$ wt %), and then the θ nullcline vanishes as seen in figure 9(*e*) ($\phi = 1.5$ wt %). In these cases,

https://doi.org/10.1017/jfm.2025.10744 Published online by Cambridge University Press

the MEP is a saddle point while the DEP is stable, corresponding to the type (C) focusing pattern. This focusing pattern agrees with the experiments for $\phi = 1.0$ and 1.5 wt % shown in figures 5(*c*) and 5(*d*).

The transition of the particle focusing from four points of the MEP to four points of the DEP with increasing ϕ is due to the immobility of the r nullcline and the shrinkage of the θ nullcline (see figure 9*a–e*). This tendency was also observed at $Re = 50$ in our previous study (Yokoyama *et al.* 2021). In that study, the conformation tensor and the force distribution on the particle surface demonstrated that, when a particle is located near the channel wall, enhanced polymer elongation observed upstream of the particle between the particle and the channel wall generates lift exerting outward (i.e. wall-induced elastic lift). Since this outward lift increases with increasing fluid elasticity, an increase in the inward lift induced by N_1 is nearly cancelled, resulting in the immobility of the r nullcline. In the present study, polymer elongation is also observed at similar locations at $Re = 20$, which supports the above explanation to the nearly immobile feature of the r nullcline seen in figure 9(*a–e*). On the other hand, at $Re = 50$, the θ nullcline crosses the r nullcline near the diagonal rather than near the midline in the transition between types (A) and (C), leading to the appearance of a pair of intersections near the diagonal (Yokoyama *et al.* 2021). These intersections represent saddle points and the DEP is changed to be stable. Thus, at $Re = 50$, particles are predicted to focus on both the MEP and DEP (the type (G) focusing pattern). This focusing pattern is also consistent with the present experimental results at $Re \approx 50$ shown in figure 7.

In figure 9(*a–e*) the r nullcline moves slightly closer to the channel centre with increasing ϕ. After vanishing the θ nullcline, however, the r nullcline moves inward rather rapidly, as seen in figure 9(*f–h*). While the r nullcline remains as a closed loop, a stable equilibrium position is the DEP (figure 9*f*, $\phi = 2.0$ wt %). This focusing pattern (type (C)) accords to the experiment for $\phi = 2.0$ wt % shown in figure 5(*e*). As ϕ increases further, the r nullcline continues to approach the channel centre, but closer to the centre along the midline than along the diagonal, as may be inferred from the r-nullcline shape in figure 9(*f*) and F_r curves in figures 8(*a*) and 8(*b*). Thus, after F_r becomes negative near the channel centre, the region of $F_r > 0$ remains near the diagonals for a while (see the F_r curve for $\phi = 2.2$ wt % in the inset of figure 8*b*), that appears as the formation of four small closed loops of the $F_r = 0$ contour near the diagonals in figure 9(*g*). In this case, F_r is negative in the whole cross-section except for inside these small loops. Along the diagonal, F_r becomes zero at two locations near the channel centre, as already seen in figure 8(*b*). The particle focusing pattern in this case corresponds to type (D), in agreement with the experiment for $\phi = 2.5$ wt % (figure 5*f*). In the numerical simulation, we obtain the type (D) focusing pattern for slightly smaller ϕ (= 2.2 wt %) and, for $\phi \geqslant 2.5$ wt %, the numerical simulation predicts that particles focus on the AEP (figure 9*h*).

A rather rapid shrinkage of the r nullcline with increasing ϕ (figure 9*e–g*) can result from a larger increase in the inward lift due to N_1 compared with an increase in the wall-induced elastic lift, directed outward. In the case of low ϕ, these two lifts increase comparably so that the increments following an increase in ϕ balance near the r nullcline (Yokoyama *et al.* 2021). This leads to the nearly unmoving r nullcline for low ϕ (figure 9*a–e*). However, for larger ϕ, as the r nullcline approaches the channel centre, i.e. away from the wall, the wall-induced elastic lift quickly decays and the inward lift due to N_1 becomes dominant. As a result, the r nullcline approaches the channel centre rather rapidly in figure 9(*e–g*) as ϕ increases.

We note here that, in figure 9(*f–h*), there are tiny regions of outward lift near the corners, which become larger with increasing ϕ. Particles located in these regions are expected to approach the corner, implying the presence of the CEP. However, in the

https://doi.org/10.1017/jfm.2025.10744 Published online by Cambridge University Press

present experiments we have not observed such particles at $Re = 20$. One of the reasons is that the area of these regions is so small that few particles are located there. When the area becomes sufficiently large for larger ϕ and a certain number of particles enter there, particle focusing on the CEP could be observed experimentally. Another reason is that the corners of the cross-section of the channel experimentally used are rounded, rather than sharply angled, as seen in figure 2(*b*), so that lift acting on the particles located near the corner can be different from the numerical computation that assumes sharp corners.

The particle focusing patterns shown in figure 9 were obtained using the FENE-P model for $\kappa = 0.15$, $Re = 20$ and $l = 100$ with El and β from table 1. These patterns can be compared with the numerical results in Yu *et al.* (2019), who adopted the Oldroyd-B model with $\kappa = 0.15$, $\widehat{Re} = 1$–100, $El = 2 \times 10^{-4}$–1 and $\beta = 0.5$. Note that in the limit of the maximum polymer length $l \to \infty$, the FENE-P model coincides with the Oldroyd-B model. At $\widehat{Re} = 50$ ($Re \approx 24$), figure 5 in their paper indicates that the focusing patterns obtained with the Oldroyd-B model are four points of the MEP at $El = 0.0002$, four points of the DEP at $El = 0.005$, four points of the DEP and four points of the CEP to give a total of eight points at $El = 0.01$, and the AEP and four points of the CEP to give a total of five points at $El = 0.02$. These focusing patterns are consistent with the present numerical results with comparable El at $Re = 20$ such as in figures 9(*b*) ($El = 0.0003$), 9(*e*) ($El = 0.0035$), 9(*f*) ($El = 0.0079$) and 9(*h*) ($El = 0.016$), though the values of β are smaller than 0.5 except for the case in figure 9(*b*) in the present computation. These similarities between the Oldroyd-B model and the FENE-P model are reasonable, considering the maximum $tr(\boldsymbol{C}) \ll l^2$ in the whole parameter range of the present study. Furthermore, the ratio $Wi/l \leqslant 3.2 \times 10^{-3} \ll 1$ (see table 1) also rationalises the similarities, as a recent study showed that for steady shear flow of the FENE-P model, the effect of finite extensibility of the polymer chains becomes significant when $Wi/l \gtrapprox 1$ (Yamani & McKinley 2023). However, there are some differences in the transition states; the bistable state of the DEP and MEP (type (G)) is obtained at $El = 0.001$ (figure 7 in Yu *et al.* 2019) instead of the sole focusing on the IEP (type (B)) in the present study as shown in figure 9(*c*), and type (D) as shown in figure 9(*g*) is absent in their study. In these transition states, subtle differences of lifts resulting from the difference in parameter values or viscoelastic models could affect the r nullcline and θ nullcline, which can change the particle focusing pattern.

The present experimental and numerical results indicate that the channel centre is unstable for $El \lessapprox 0.01$ and it is stable for $El \gtrapprox 0.01$ at low Re (figures 7–9). If the lift acting on the particle is expressed as the summation of the inertial lift F_{Ir} and the fluid elasticity-induced lift F_{Er} such as $F_r = F_{Ir} + F_{Er}$, this result implies that $F_r > 0$ for $El \lessapprox 0.01$, $F_r < 0$ for $El \gtrapprox 0.01$ and that $F_r = F_{Ir} + F_{Er} \approx 0$ at $El = 0.01$ near the channel centre. Note that $F_r \approx |\boldsymbol{F}|$, since $F_\theta \approx 0$ near the centre (figure 8*c*). According to Di Carlo *et al.* (2009), the inertial lift can be expressed in a dimensional form as

$$F_{Ir}^* = f_I \rho^* U^{*2} d^{*2} \kappa = f_I \mu^* U^* d^* Re_p, \tag{3.1}$$

where f_I is a dimensionless function of the particle position. On the other hand, the radial component of the fluid elasticity-induced lift due to N_1^* can be expressed in terms of a dimensionless coefficient f_E as

$$F_{Er}^* = f_E d^{*3} \frac{\partial N_1^*}{\partial r^*} \tag{3.2}$$

(Tehrani 1996). Since $N_1^* = 2\mu^*(1-\beta)\lambda^* \dot{\gamma}^{*2}$ for a Poiseuille flow of Boger fluids (James 2009), we have

https://doi.org/10.1017/jfm.2025.10744 Published online by Cambridge University Press

$$F^*_{Er} = f_E \mu^* U^* d^* Wi \kappa^2 1024(1-\beta)\frac{r^*}{D^*}. \tag{3.3}$$

Then, $F^*_r = F^*_{Ir} + F^*_{Er} \approx 0$ leads to

$$F^*_r = \mu^* U^* d^* Re_p \left[f_I + 1024 f_E El(1-\beta)\frac{r^*}{D^*} \right] \approx 0 \tag{3.4}$$

near the channel centre. From the numerically obtained curve of F_r on the diagonal for $\phi = 0$, the dash-dotted line in figure 8(b) gives $f_I = F^*_{Ir}/\rho^* U^{*2} d^{*2} \kappa \approx 1.1 r^*/D^*$. Inserting $El = 0.01$ and $\beta = 0.14$ ($\phi = 2.2$ wt %) into (3.4), we have $f_E \approx -0.125$. Thus, it is concluded that the fluid elasticity-induced lift near the channel centre is given by (3.3) with this value. Furthermore, if we rewrite (3.3) as

$$F^*_{Er} = \widetilde{f}_E \rho^* U^{*2}_{max} d^{*2} \kappa El(1-\beta)\frac{r^*}{D^*} \quad (\widetilde{f}_E \equiv 256 f_E), \tag{3.5}$$

then, comparison with (3.1) in Li *et al.* (2015) derived from Ho & Leal (1976) for a second-order fluid gives

$$\widetilde{f}_E = -\frac{40}{3}\pi. \tag{3.6}$$

The present value $\widetilde{f}_E = -32$ is comparable to (3.6). The slight difference is acceptable, considering that Ho & Leal (1976) treated a small particle in a 2-D shear flow.

Hitherto, the effect of the elasticity number El on particle focusing behaviour has mainly been studied. Here, the effect of the viscosity ratio β is briefly considered. Figure 10 shows the lift map, equilibrium positions, nullclines and particle trajectories at various β for $El = 0.0003$ and 0.0012. The cases of $\beta = 0.7$ in figure 10(a) and $\beta = 0.4$ in figure 10(b) represent those of $\phi = 0.5$ wt % and 1.0 wt %, respectively (table 1). Figures 10(a) and 10(b) both indicate that, as β decreases, the closed loop of the θ nullcline gradually shrinks, enhancing the effect of fluid elasticity. In figure 10(a) the stability of equilibrium positions is unchanged, whereas, in figure 10(b), stable equilibrium positions transition from the MEP, to the IEP and then the DEP, with decreasing β. Thus, when ϕ increases, both increasing El and decreasing β intensify the effect of fluid elasticity. It seems that El affects the migration behaviours more significantly than β, as far as the parameter range examined, but β could change the stability of equilibrium positions when close to the transition state, as shown in figure 10(b).

4. Conclusions

In the present study we have experimentally and numerically investigated the inertial migration of neutrally buoyant spherical particles in viscoelastic fluids flowing through square channels. In the experiments, using dilute aqueous solutions of PVP with various concentrations that have nearly constant viscosities irrespective of the shear rate, we measured the distribution of particles in downstream cross-sections for Re up to 100 and El up to 0.07 (or the PVP concentration up to 4 wt %) at $\kappa = 0.15$. Depending on Re and El (PVP concentration), there are a variety of particle focusing patterns and equilibrium positions. In addition to the MEP, DEP, CEP and AEP, this study demonstrates the presence of a new equilibrium position located at an intermediate position between the midline and the diagonal (IEP) and several types of multistable states of different equilibrium positions. As the fluid elasticity increases at a constant Re (= 20), the focusing positions of particles shift from the midline (MEP) to the diagonal (DEP) in the azimuthal direction first and then inward in the radial direction to the channel centre (AEP). The AEP

https://doi.org/10.1017/jfm.2025.10744 Published online by Cambridge University Press

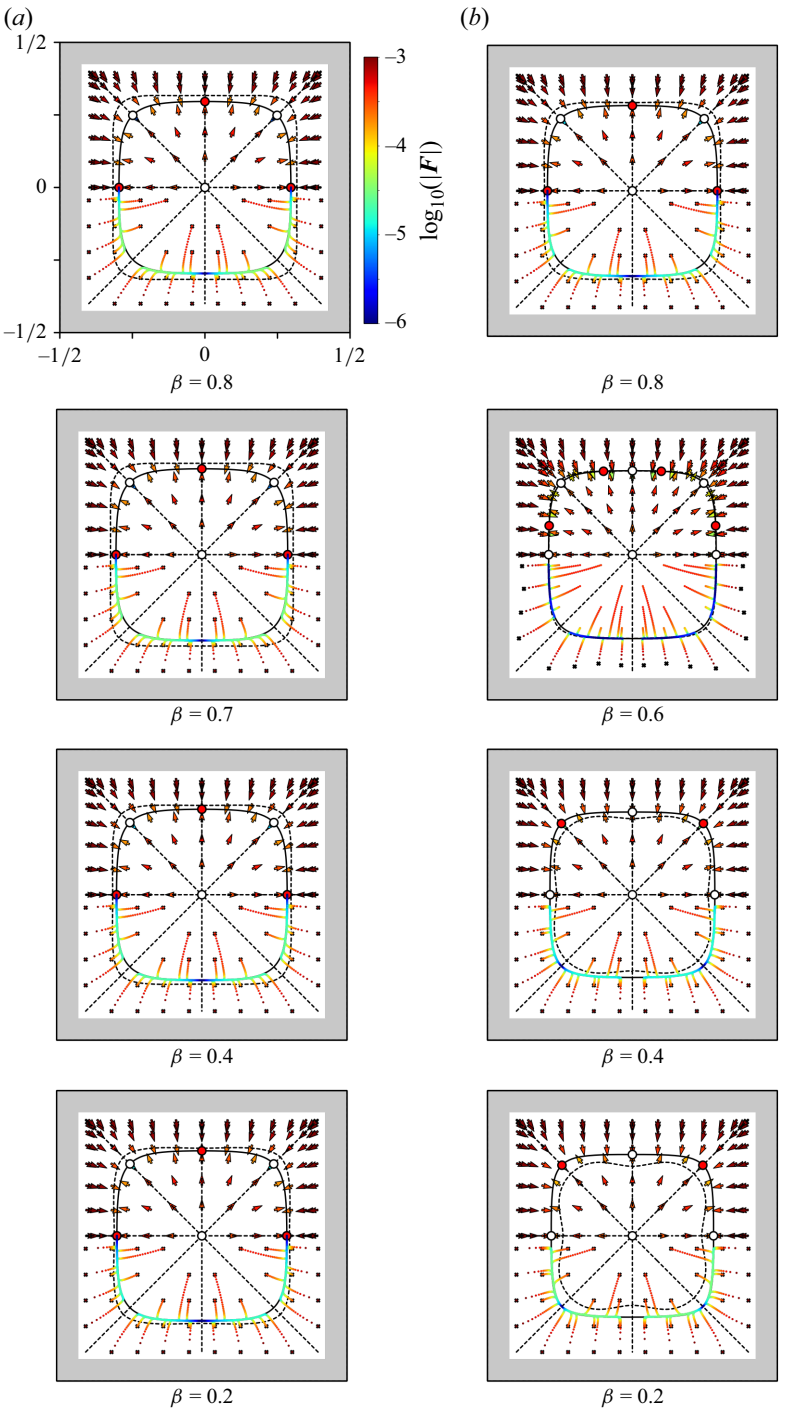


Figure 10. Effects of the viscosity ratio β: numerical results of lifts, equilibrium positions, r nullcline (solid lines), θ nullcline (dashed lines) and particle trajectories at $Re = 20$ for (*a*) $El = 0.0003$ and (*b*) $El = 0.0012$.

https://doi.org/10.1017/jfm.2025.10744 Published online by Cambridge University Press

becomes stable for $El \gtrapprox 0.01$. The present study is the first to experimentally substantiate the critical Re above which the AEP is stable. Numerical simulations based on the FENE-P model reproduced successfully these focusing patterns with the parameter values equal or close to the rheological measurements. To the best of the authors' knowledge, such agreements between the numerical and experimental results have been rarely reported, because viscoelastic fluids generally have complex rheological properties and, thus, viscoelastic flows are substantially complicated. As far as the parameter range studied, the PVP solutions are well modelled by the FENE-P fluid with the elasticity number El and the viscosity ratio β estimated from the rheological measurements. Quantitative comparison between the experimental and numerical results is further required, and it is our future work to evaluate the rheological properties of the PVP solutions in more detail and incorporate them into the numerical model, which is quite challenging (Dubief, Terrapon & Hof 2023). The present study shows that an increase in the PVP concentration intensifies the effect of fluid elasticity by increasing El and decreasing β, and the transitions of particle focusing patterns can be accounted for by a competition between the inertial lift and the fluid elasticity-induced lift, which is composed of that due to N_1, directed towards the lower shear, and the wall-induced elastic lift, generated by the elongation of polymers in the region between the particle and the channel wall. In particular, the experimentally observed stability of the AEP is well reproduced by numerical simulations, and based on this result, a quantitative expression of the elasticity-induced lift is presented near the channel centre. This study provides a concrete example showing that particle focusing in viscoelastic fluids can be well described by the lift due to the fluid elasticity when shear thinning and secondary flow are weak, and elucidating the effect of fluid elasticity on the suspended particle focusing presents the potential to understand the effects of shear thinning (thickening) and secondary flow by isolating the effect of fluid elasticity from complicated behaviours in viscoelastic fluids. It helps to disentangle the complex dynamics of the viscoelastic flows.

Supplementary material. Supplementary material is available at https://doi.org/10.1017/jfm.2025.10744.

Acknowledgements. The authors are grateful to Mr T. Nakata for his technical assistance with the experiment. The numerical computation was carried out using large-scale computer systems at Research Institute for Information Technology, Kyushu University, and at the Cybermedia Center, Osaka University. The viscosity of the PVP solutions was measured using a rheometer at ORIST (Osaka Research Institute of Industrial Science and Technology).

Funding. This research was partially supported by JSPS KAKENHI Grant Numbers JP20H02072 and JP24K00809.

Declaration of interests. The authors report no conflict of interest.

References

Abbas, M., Magaud, P., Gao, Y. & Geoffroy, S. 2014 Migration of finite sized particles in a laminar square channel flow from low to high Reynolds numbers. *Phys. Fluids* **26**, 123301.

Abdel Azim, A.-A.A., Tenhu, H., Maerta, J. & Sundholm, F. 1992 Flexibility and hydrodynamic properties of poly(vinylpyrrolidone) in non-ideal solvents. *Polym. Bull.* **29**, 461–467.

Asmolov, E.S.1999 The inertial lift on a spherical particle in a plane Poiseuille flow at large channel Reynolds number. *J. Fluid Mech.* **381**, 63–87.

Balci, N., Thomases, B., Renardy, M. & Doering, C.R. 2011 Symmetric factorization of the conformation tensor in viscoelastic fluid models. *J. Nonnewton. Fluid Mech.* **166**, 546–553.

Bhagat, A.A.S., Kuntaegowdanahalli, S.S. & Papautsky, I. 2008 Enhanced particle filtration in straight microchannels using shear-modulated inertial migration. *Phys. Fluids* **20**, 101702.

Choi, Y., Seo, K. & Lee, S. 2011 Lateral and cross-lateral focusing of spherical particles in a square microchannel. *Lab Chip* **11**, 460–465.

https://doi.org/10.1017/jfm.2025.10744 Published online by Cambridge University Press

CLASEN, C., PLOG, J.P., KULICKE, W.-M., OWENS, M., MACOSKO, C., SCRIVEN, L.E., VERANI, M. & MCKINLEY, G.H. 2006 How dilute are dilute solutions in extensional flows? *J. Rheol.* **50**, 849–881.
DEL GUIDICE, F., ROMEO, G., D'AVINO, G., GRECO, F., NETTI, P. & MAFFETTONE, P.L. 2013 Particle alignment in a viscoelastic liquid flowing in a square-shaped microchannel. *Lab Chip* **13**, 4263–4271.
DEL GIUDICE, F., D'AVINO, G., GRECO, F., MAFFETTONE, P.L. & SHEN, A.Q. 2018 Fluid viscoelasticity drives self-assembly of particle trains in a straight microfluidic channel. *Phys. Rev. Appl* **10**, 064058.
DI CARLO, D. 2009 Inertial microfluidics. *Lab Chip* **9**, 3038–3046.
DI CARLO, D., EDD, J.F., HUMPHRY, K.J., STONE, A.H. & TONER, M. 2009 Particle segregation and dynamics in confined flows. *Phys. Rev. Lett.* **102**, 094503.
DI CARLO, D., IRIMA, D., TOMPKINS, R.G. & TONER, M. 2007 Continuous inertial focusing, ordering, and separation of particles in microchannels. *Proc. Natl. Acad. Sci. USA* **104**, 18892–18897.
D'AVINO, G. & MAFFETTONE, P.L. 2015 Particle dynamics in viscoelastic liquids. *J. Nonnewton. Fluid Mech.* **215**, 80–104.
D'AVINO, G., GRECO, F. & MAFFETTONE, P.L. 2017 Particle migration due to viscoelasticity of the suspending liquid and its relevance in microfluidic devices. *Annu. Rev. Fluid Mech.* **49**, 341–360.
D'AVINO, G. & MAFFETTONE, P.L. 2020 Numerical simulations on the dynamics of trains of particles in a viscoelastic fluid flowing in a microchannel. *Meccanica* **55**, 317–330.
DINIC, J., JIMENEZ, L.N. & SHARMA, V. 2017 Pinch-off dynamics and dripping-onto-substrate (DoS) rheometry of complex fluids. *Lab Chip* **17**, 460–473.
DUBIEF, Y., TERRAPON, V.E. & HOF, B. 2023 Elasto-inertial turbulence. *Annu. Rev. Fluid Mech.* **55**, 675–705.
FRANCO-GÓMEZ, A., ONUKI, H., YOKOYAMA, Y., NAGATSU, Y. & TAGAWA, Y. 2021 Effect of liquid elasticity on the behaviour of high-speed focused jets. *Exp. Fluids* **62**, 41.
GAUTHIER, F., GOLDSMITH, H.L. & MASON, S.G. 1971 Particle motions in non-Newtonian media. II. Poiseuille flow. *Trans. Soc. Rheol* **15**, 297–330.
HERRCHEN, M. & ÖTTINGER, H.C. 1997 A detailed comparison of various FENE dumbbell models. *J. Non-Newton. Fluid Mech.* **68**, 17–42.
HO, B.P. & LEAL, L.G.1974 Inertial migration of rigid spheres in two-dimensional unidirectional flow. *J. Fluid Mech.* **65**, 365–400.
HO, B.P. & LEAL, L.G. 1976 Migration of rigid spheres in a two-dimensional unidirectional shear flow of a second-order fluid. *J. Fluid Mech.* **76**, 783–700.
HU, X., LIN, P., LIN, J., ZHU, Z. & YU, Z. 2022 On the polydisperse particle migration and formation of chains in a square channel flow of non-Newtonian fluids. *J. Fluid Mech.* **936**, A5.
HU, X., LIN, J., ZHU, Z., YU, Z., LIN, Z. & LI, X. 2024 Elasto-inertial focusing and rotating characteristics of ellipsoidal particles in a square channel flow of Oldroyd-B viscoelasitc fluids. *J. Fluid Mech.* **997**, A32.
HUMPHRY, K.J., KULKARNI, P.M., WEITZ, D.A., MORRIS, J.F. & STONE, H.A. 2010 Axial and lateral particle ordering in finite Reynolds number channel flows. *Phys. Fluids* **22**, 081703.
HUR, S.C., TSE, H.T.K. & DI CARLO, D. 2010 Sheathless inertial cell ordering for extreme throughput flow cytometry. *Lab Chip* **10**, 274–280.
JAMES, D.F. 2009 Boger fluids. *Annu. Rev. Fluid Mech.* **41**, 129–142.
JOHN, T.P., POOLE, R.J., KOWALSKI, A.J. & FONTE, C.P. 2024 A comparison between the FENE-P and sPTT constitutive models in large-amplitude oscillatory shear. *J. Fluid Mech.* **979**, A10.
KAHKESHANI, S., HADDADI, H. & DI CARLO, D. 2016 Preferred interparticle spacings in trains of particles in inertial microchannel flows. *J. Fluid Mech.* **786**, R3.
KAJISHIMA, T., TAKIGUCHI, S., HAMASAKI, H. & MIYAKE, Y. 2001 Turbulence structure of particle-laden flow in a vertical plane channel due to vortex shedding. *JSME J. B* **44**, 526–535.
KALYAN, S., TORABI, C., KHOO, H., SUNG, H.W., CHOI, S.-E., WANG, W., TREUTLER, B., KIM, D. & HUR, S.C. 2021 Inertial microfluidics enabling clinical research. *Micromachines* **12**, 257.
KAMLI, M., GUETTARI, M. & TAJOURI, T. 2023 Structure of polyvinylpyrrolidone in water/ethanol mixture in dilute and semi-dilute regimes: roles of solvents mixture composition and polymer concentration. *J. Molecular Liquids* **382**, 122014.
KARNIS, A. & MASON, S.G. 1966 Particle motions in sheared suspensions. XIX. Viscoelastic media. *Trans. Soc. Rheol.* **10**, 571–592.
KAZEROONI, H.T., FORNARI, W., HUSSONG, J. & BRANDT, L. 2017 Inertial migration in dilute and semidilute suspensions of rigid particles in laminar square duct flow. *Phys. Rev. Fluids* **2**, 084301.
KIM, B. & KIM, J.M. 2016 Elasto-inertial particle focusing under the viscoelastic flow of DNA solution in a square channel. *Biomicrofluidics* **10**, 024111.
KIM, J.Y., AHN, S.W., LEE, S.S. & KIM, J.M. 2012 Lateral migration and focusing of colloidal particles and DNA molecules under viscoelastic flow. *Lab Chip* **12**, 2807–2814.

https://doi.org/10.1017/jfm.2025.10744 Published online by Cambridge University Press

KIM, Y.W. & YOO, J.Y. 2008 The lateral migration of neutrally-buoyant spheres transported through square microchannels. *J. Micromech. Microeng.* **18**, 065015.

LEE, S., KIM, H. & YANG, S. 2023 Microfluidic label-free hydrodynamic separation of blood cells: recent developments and future perspectives. *Adv. Mater. Technol.* **8**, 2201425.

LESHANSKY, A.M., BRANSKY, A., KORIN, N. & DINNAR, U. 2007 Tunable nonlinear viscoelastic 'focusing' in a microfluidic device. *Phys. Rev. Lett.* **98**, 234501.

LI, G., MCKINLEY, G.H. & ARDEKANI, A.M. 2015 Dynamics of particle migration in channel flow of viscoelastic fluids. *J. Fluid Mech.* **785**, 486–505.

LIM, E.J., OBER, T.J., EDD, J.F., DESAI, S.P., NEAL, D., BONG, K.W., DOYLE, P.S., MCKINLEY, G.H. & TONER, M. 2014 Inertio-elastic focusing of bioparticles in microchannels at high throughput. *Nature Comm.* **5**, 4120.

LU, X., LIU, C., HU, G. & XUAN, X. 2017 Particle manipulations in non-Newtonian microfluidics: a review. *J. Colloid Interface Sci* **500**, 182–201.

MATAS, J.-P., GLEZER, V., GUAZZELLI, E. & MORRIS, J.F. 2004*a* Trains of particles in finite-Reynolds-number pipe flow. *Phys. Fluids* **16**, 4192–4195.

MATAS, J.-P., MORRIS, J.F. & GUAZZELLI, E. 2004*b* Inertial migration of rigid spherical particles in Poiseuille flow. *J. Fluid Mech.* **515**, 171–195.

MATAS, J.-P., MORRIS, J.F. & GUAZZELLI, E. 2004*c* Lateral forces on a sphere. *Oil Gas Sci. Technol.-Rev. JFP* **59**, 59–70.

MATAS, J.-P., MORRIS, J.F. & GUAZZELLI, E. 2009 Lateral force on a rigid sphere in large-inertia laminar pipe flow. *J. Fluid Mech.* **621**, 59–67.

MATEL, J.M. & TONER, M. 2014 Inertial focusing in microfluidics. *Annu. Rev. Biomed. Eng* **16**, 371–396.

MIURA, K., ITANO, T. & SUGIHARA-SEKI, M. 2014 Inertial migration of neutrally buoyant spheres in a pressure-driven flow through square channels. *J. Fluid Mech.* **749**, 320–330.

NAKAGAWA, N., YABU, T., OTOMO, R., KASE, A., MAKINO, M., ITANO, T. & SUGIHARA-SEKI, M. 2015 Inertial migration of a spherical particle in laminar square channel flows from low to high Reynolds numbers. *J. Fluid Mech.* **779**, 776–793.

PENG, S., TANG, T., LI, J., ZHANG, M. & YU, P. 2023 Numerical study of viscoelastic upstream instability. *J. Fluid Mech.* **959**, A16.

PROHM, C. & STARK, H. 2014 Feedback control of inertial microfluidics using axial control forces. *Lab Chip* **14**, 2115.

PURNODE, B. & CROCHET, M.J. 1998 Polymer solution characterization with the FENE-P model. *J. Non-Newton. Fluid Mech.* **77**, 1–20.

RAOUFI, M.A., MASHHADIAN, A., NIAZMAND, H., ASADNIA, M., RAZMJOU, A. & WARKIANI, M.E. 2019 Experimental and numerical study of elasto-inertial focusing in straight channels. *Biomicrofluidics* **13**, 034103.

RAZAVI BAZAZ, S., MASHHADIAN, A., EHSANI, A., SAHA, S.C., KRÜGER, T. & WARKIANI, M.E. 2020 Computational inertial microfluidics: a review. *Lab Chip* **20**, 1023.

RUBIO, A., VEGA, E.J., GAÁN-CALVO, A.M. & MONTANERO, J.M. 2022 Unexpected stability of micrometer weakly viscoelastic jets. *Phys. Fluids* **34**, 062014.

SCHONBERG, J.A. & HINCH, E.J. 1989 Inertial migration of a sphere in Poiseuille flow. *J. Fluid Mech.* **203**, 517–524.

SEGRÉ, G. & SILBERBERG, A. 1961 Radial particle displacements in Poiseuille flow of suspensions. *Nature* **189**, 209–210.

SEGRÉ, G. & SILBERBERG, A. 1962 Behaviour of macroscopic rigid spheres in Poiseuille flow. Part 2. Experimental results and interpretation. *J. Fluid Mech.* **14**, 136–157.

SEO, K.W., KANG, Y.J. & LEE, S.J. 2014 Lateral migration and focusing of microspheres in a microchannel flow of viscoelastic fluids. *Phys. Fluids* **26**, 063301.

SHICHI, H., YAMASHITA, H., SEKI, J., ITANO, T. & SUGIHARA-SEKI, M. 2017 Inertial migration regimes of spherical particles suspended in submillimeter square tube flows. *Phys. Rev. Fluids* **2**, 044201.

STEINBERG, Z. 2021 Elastic turbulence: an experimental view on inertialess random flow. *Ann. Rev. Fluid Mech.* **53**, 27–58.

STOECKLEIN, D. & DI CARLO, D. 2019 Nonlinear microfluidics. *Anal. Chem.* **91**, 296–314.

SUR, S. & ROTHSTEIN, J. 2018 Drop breakup dynamics of dilute polymer solutions: effect of molecular weight, concentration, and viscosity. *J. Rheol.* **62**, 1245–1259.

TANG, W., ZHU, S., JIANG, D., ZHU, L., YANG, J. & XIANG, N. 2020 Channel innovations for inertial microfluidics. *Lab Chip* **20**, 3485.

TEHRANI, M.A. 1996 An experimental study of particle migration in pipe flow of viscoelastic fluids. *J. Rheol.* **40**, 1057–1077.

https://doi.org/10.1017/jfm.2025.10744 Published online by Cambridge University Press

UDONO, H. 2020 Numerical investigations of strong hydrodynamic interaction between neighboring particles inertially driven in microfluidic flows. *Adv. Powder Technol.* **31**, 4107–4118.

VILLONE, M.M., D'AVINO, G., HULSEN, M.A., GRECO, F. & MAFFETTONE, P.L. 2013 Particle motion in square channel flow of a viscoelastic liquid: migration vs. secondary flow. *J. Non-Newton. Fluid Mech.* **195**, 1–8.

YAMANI, S. & MCKINLEY, G.H. 2023 Master curves for FENE-P fluids in steady shear flow. *J. Non-Newton. Fluid Mech.* **313**,104944, 104944.

YAMASHITA, H., ITANO, T. & SUGIHARA-SEKI, M. 2019 Bifurcation phenomena on the inertial focusing of a neutrally buoyant spherical particle suspended in square duct flows. *Phys. Rev. Fluids* **4**, 124307.

YANG, S., KIM, J.Y., LEE, S.J., LEE, S.S. & KIM, J.M. 2011 Sheathless elasto-inertial particle focusing and continuous separation in a straight rectangular microchannel. *Lab Chip* **11**, 266–273.

YANG, S., LEE, S.S., AHN, S.W., KANG, K., SHIM, W., LEE, G., HYUN, K. & KIM, J.M. 2012 Deformability-selective particle entrainment and separation in a rectangular microchannel using medium viscoelasticity. *Soft Matter* **8**, 5011–5019.

YOKOYAMA, N., YAMASHITA, H., HIGASHI, K., MIKI, Y., ITANO, T. & SUGIHARA-SEKI, M. 2021 Variation of focusing patterns of laterally migrating particles in a square-tube flow due to non-Newtonian elastic force. *Phys. Rev. Fluids* **6**, L072301.

YU, Z., WANG, P., LIN, J. & HU, H.H. 2019 Equilibrium positions of the elasto-inertial particle migration in rectangular channel flow of Oldroyd-B viscoelastic fluids. *J. Fluid Mech.* **868**, 316–340.

YUAN, D., ZHAO, Q., YAN, S., TANG, S.-Y., ALICI, G., ZHANG, J. & LI, W. 2018 Recent progress of particle migration in viscoelastic fluids. *Lab Chip* **18**, 551.

ZHANG, J., YAN, S., YUAN, D., ALICI, G., NGUYEN, N.-T., WARKIANI, M.E. & LI, W. 2016 Fundamentals and applications of inertial microfluidics: a review. *Lab Chip* **16**, 10.

ZHANG, T. *et al.*et al. 2024 Passive microfluidic devices for cell separation. *Biotechnol. Adv* **71**, 108317.

ZHOU, J. & PAPAUTSKY, I. 2020 Viscoelastic microfluidics: progress and challenges. *Microsys. Nanoeng.* **6**, 113.

https://doi.org/10.1017/jfm.2025.10744 Published online by Cambridge University Press